Prograde infiltration of Cl-rich fluid into the granulitic continental crust from a collision zone in East Antarctica (Perlebandet, Sør Rondane Mountains)

Tetsuo Kawakami[1,*], Fumiko Higashino[1,2], Etienne Skrzypek[1], M. Satish-Kumar[3], Geoffrey Grantham[4], Noriyoshi Tsuchiya[5], Masahiro Ishikawa[6], Shuhei Sakata[1], Takafumi Hirata[1]

1   Department of Geology and Mineralogy, Graduate School of Science, Kyoto University, Kitashirakawa-Oiwake-cho, Sakyo-ku, Kyoto 606-8502, Japan

2   Research Fellow of Japan Society for the Promotion of Science

3   Department of Geology, Faculty of Science, Niigata University, 2-8050 Ikarashi, Nishi-ku, Niigata 950-2181, Japan

4   Department of Geology, University of Johannesburg, PO Box 524, Auckland Park, 2006, South Africa

5   Department of Geoscience and Technology, Graduate School of Engineering, Tohoku University, Aramaki, Aoba-ku, Sendai 980-9570, Japan

6   Graduate School of Environment and Information Sciences, Yokohama National University, Tokiwadai, Hodogaya-ku, Yokohama 240-8501, Japan

19

20   *Corresponding author; t-kawakami@kueps.kyoto-u.ac.jp

21

22

23   **Abstract**

24   Utilizing microstructures of Cl-bearing biotite in pelitic and felsic metamorphic rocks, the timing

25   of Cl-rich fluid infiltration is correlated with the pressure-temperature-time (P-T-t) path of upper

26   amphibolite- to granulite-facies metamorphic rocks from Perlebandet, Sør Rondane Mountains

27   (SRM), East Antarctica. Microstructural observation indicates that the stable Al_2SiO_5 polymorph

28   changed from sillimanite to kyanite + andalusite + sillimanite, and P-T estimates from

29   geothermobarometry point to a counterclockwise P-T path characteristic of the SW terrane of the

30   SRM. *In situ* laser ablation inductively coupled plasma mass spectrometry for U-Pb dating of zircon

31   inclusions in garnet yielded ca. 580 Ma, likely representing the age of garnet-forming metamorphism

32   at Perlebandet.

33   Inclusion-host relationships among garnet, sillimanite, and Cl-rich biotite (Cl > 0.4 wt%) reveal

34   that formation of Cl-rich biotite took place during prograde metamorphism in the sillimanite stability

35   field. This process probably predated partial melting consuming biotite (Cl = 0.1-0.3 wt%). This was

36   followed by retrograde, moderately Cl-bearing biotite (Cl = 0.1-0.3 wt%) replacing garnet. Similar

37 timings of Cl-rich biotite formation in different samples, and similar $f(H_2O)/f(HCl)$ values of

38 coexisting fluid estimated for each stage can be best explained by prograde Cl-rich fluid infiltration.

39 Fluid-present partial melting at the onset of prograde metamorphism probably contributed to elevate

40 the Cl concentration (and possibly salinity) of the fluid, and consumption of the fluid resulted in the

41 progress of dehydration melting. The retrograde fluid was released from crystallizing Cl-bearing

42 partial melts or derived externally. The prograde Cl-rich fluid infiltration in Perlebandet presumably

43 took place at the uppermost part of the footwall of the collision boundary. Localized distribution of

44 Cl-rich biotite and hornblende along large-scale shear zones and detachments in the SRM supports

45 external input of Cl-rich fluids through tectonic boundaries during continental collision.

46

47 Keywords: fluid, brine, partial melting, Al_2SiO_5 polymorphs, chlorine, continental collision

48

49 **Introduction**

50 Low water activity fluids have been recognized as the major fluid species present under granulite

51 facies conditions prevailing in the lower continental crust (Aranovich et al., 1987; Newton et al., 1998;

52 Touret and Huizenga, 2011). Under such conditions, brines can immiscibly coexist with CO_2-rich

53 fluids (Heinrich, 2007). Direct evidence of highly saline brine, such as fluid inclusions (van den Berg

54 and Huizenga, 2001) and/or salt crystals (e.g., Markl and Bucher, 1998) have been reported, although

55   they are relatively uncommon. Rare preservation of brines as fluid inclusions is attributed to the low

56   viscosity and low wetting angle of brines (Watson and Brenan, 1987; Holness, 1997) that make it easy

57   for brine to escape the rock. In addition, steep isochores of $NaCl-H_2O$ fluids in pressure-temperature

58   (*P-T*) space result in gross overpressurization of brine inclusions during heating and decrepitation or

59   implosion during isobaric cooling (Touret et al., 2016). These features probably hindered

60   understanding of the timing and spatial distribution of brines in high-grade metamorphic terranes.

61   The presence of Cl-rich biotite, hornblende and apatite is often taken as evidence for the presence

62   of Cl-bearing fluids and brines (e.g., Harlov and Förster, 2002; Higashino et al., 2013a; Safonov et al.,

63   2014). These minerals are known to incorporate Cl in place of OH in their crystal structures when they

64   exchange with Cl-bearing fluids (e.g., Munoz and Swenson, 1981; Kullerud, 1996). Data on Cl

65   partitioning between fluids and these minerals is available (e.g., Zhu and Sverjensky, 1991; 1992;

66   Mathez and Webster, 2005); the $f(H_2O)/f(HCl)$ ratio of the coexisting fluid can be estimated from the

67   composition of biotite and apatite (e.g., Selby and Nesbitt, 2000). In partially molten, migmatitic

68   pelitic gneisses, Cl-rich biotite may coexist with nanogranite/felsite inclusions (Kawakami et al.,

69   2016; see Hiroi et al. (2014) for 'felsite inclusions'), and thus not only subsolidus Cl-rich aqueous

70   fluid infiltration but also processes involving partial melting can lead to the formation of Cl-rich

71   biotite.

72   This study aims to correlate the reconstructed *P-T-t* path with partial melting and Cl-rich fluid

73　　infiltration events using microstructural observations pointing to several stages of Cl-bearing biotite

74　　formation in pelitic and felsic gneisses from Perlebandet (western Sør Rondane Mountains (SRM),

75　　East Antarctica). We discuss multiple Cl-bearing fluid infiltration events in the SRM. Mineral

76　　abbreviations are after Kretz (1983).

77

78　　**Geological setting**

79　　**The Sør Rondane Mountains**

80　　　　In the SRM (22º-28ºE, 71.5º-72.5ºS) of eastern Dronning Maud Land, East Antarctica (Fig. 1a),

81　　the granulite facies lower continental crust of a continental collision setting is widely exposed

82　　(Shiraishi et al., 1991; Asami et al., 1992). The SRM are thought to be a part of the collision zone

83　　between East and West Gondwana during the ca. 750–620 Ma 'East African-Antarctic Orogeny

84　　(EAAO)' (Jacobs et al., 2003) and are also affected by the ca. 570–500 Ma 'Kuunga Orogeny' (Meert,

85　　2003). Apparent depositional ages of metacarbonate rocks from Balchenfjella, Brattnipene, Menipa

86　　and Tanngarden regions in the SRM (Fig. 1b) are estimated as late-Tonian and early-Cryogenian age

87　　(880–850 Ma and 820–790 Ma) based on a Sr isotope study (Otsuji et al., 2013). Protoliths of

88　　metacarbonates are considered to have been deposited in the Mozambique Ocean that separated the

89　　continental blocks that amalgamated to form Gondwana (Otsuji et al., 2013).

90　　　　The SRM is divided into the NE and SW terranes which are separated by a gently N- to

91   NE-dipping mylonite zone named the Main Tectonic Boundary (MTB; Osanai et al., 2013) (Fig. 1b).

92   The NE terrane is mainly composed of amphibolite- to granulite-facies metamorphic rocks of pelitic,

93   psammitic, and intermediate compositions (Shiraishi and Kojima, 1987; Asami and Shiraishi, 1987;

94   Grew et al., 1989) showing clockwise *P-T* paths (Osanai et al., 2013; Grantham et al., 2013). In

95   contrast, the SW terrane is composed of granulite- to greenschist-facies rocks with a large volume of

96   meta-tonalite (Fig. 1b; Shiraishi et al., 2008; Kamei et al., 2013), showing counterclockwise *P-T* paths

97   (Adachi et al., 2013; Baba et al., 2013). U-Pb ages of detrital zircon are also different between these

98   two terranes; detrital zircons older than 1200 Ma are absent from the SW terrane (Osanai et al., 2013;

99   Kitano et al., 2016). Based on these observations, the two different *P-T* paths in these adjoining

100   terranes are explained by the collision between these two terranes, with the NE-terrane thrusted over

101   the SW-terrane during the EAAO at 650-600 Ma, followed by amphibolite-facies metamorphism at

102   ca. 570 Ma (Osanai et al., 2013). A SE-dipping ductile extensional shear zone termed the Balchen

103   Detachment Fault (BDF) structurally divides Balchenfjella (Fig. 1b), and the southeastward

104   movement of the Berrheia unit (hanging wall side) with respect to the Gropeheia unit (footwall side) is

105   inferred to represent an extensional deformation phase between ca. 600 Ma and ca. 549 Ma (Ishikawa

106   et al., 2013), which is interpreted to result from extensional collapse after crustal overthickening.

107   The Main Shear Zone (Kojima and Shiraishi, 1986; Fig. 1b) that defines the boundary between

108   older meta-tonalite and amphibolite-facies metamorphic rocks in the SW-terrane was inferred to have

109   limited tectonic significance by Osanai et al. (2013). However, Ruppel et al. (2015) interpreted it to be

110   a large-scale late Pan-African strike-slip structure of ca. 560-530 Ma, representing an important

111   lithotectonic boundary separating East African affinities from 'Indo-Antarctic' Rayner-age affinities

112   presumably close to the eastern margin of the EAAO (Ruppel et al., 2015).

113   The SRM is also interpreted to be a part of the hanging wall of a mega-nappe complex which

114   formed through continental collision between northern and southern Gondwana during the Kuunga

115   Orogeny at 580–540 Ma (Grantham et al., 2008; 2013), as supported by the data from part of the NE

116   terrane (Balchenfjella and Austhameren; Fig. 1b).

117   In the SRM, Cl-rich biotite, apatite and hornblende have been described in felsic and mafic

118   gneisses along the large scale shear zones and tectonic boundaries which extend over 200 km

119   (Higashino et al., 2013a; 2013b; 2015a; Fig. 1b). In eastern SRM (Balchenfjella; Fig. 1b), Cl-rich

120   biotite and apatite in pelitic gneisses have been interpreted to have resulted from interaction with a

121   Cl-rich fluid or melt that was present at near peak metamorphic condition of ca. 0.8 GPa and 800 $^{\circ}$C

122   (Higashino et al., 2013a). In the central SRM (Brattnipene; Fig. 1b), Cl-rich hornblende and biotite are

123   formed along garnet-hornblende veins, and 'diffusion-like' profiles of Cl content in hornblende and

124   biotite decreasing from the vein towards the wall rock are observed (Higashino et al., 2015b). Mass

125   balance analysis revealed that elements mobile in brines rather than in melts were added to the wall

126   rock, suggesting that brine infiltration produced the garnet-hornblende veins in Brattnipene

127   (Higashino et al., 2015b).

128   In addition to these Cl-rich minerals in metamorphic rocks, magmatic hornblende and biotite

129   show relatively high Cl contents in some granitoids in the SRM. Li et al. (2003, 2007) reported

130   0.28-0.32 wt.% Cl in hornblende from the Dufek granite, and 0.31-0.41 wt.% Cl in hornblende and

131   0.21-0.59 wt.% Cl in biotite from the Pingvinane granite (Fig. 1b). The U-Pb zircon age determined by

132   SHRIMP or laser ablation inductively coupled plasma mass spectrometry (LA-ICPMS) is 619 ± 7 Ma

133   (Li et al., 2006) and 637 ± 6 Ma (Elburg et al., 2016) for the Dufek granite, and 506 ± 4 Ma (Elburg et

134   al., 2016) for the Pingvinane granite.

135

136   **Perlebandet**

137   Perlebandet is one of the westernmost nunataks in the SRM, where granulite facies layered

138   gneisses are exposed (Fig. 1c). It is a key area to constrain the location of the MTB, and has been

139   considered to belong to the NE terrane (Osanai et al., 2013) in the lack of detailed information of *P-T*

140   path of this area. However, Perlebandet is interpreted to be part of the SW terrane on the basis of

141   magnetic surveys (Mieth et al., 2014).

142   The main lithologies observed in Perlebandet are garnet-biotite (Grt-Bt) gneiss,

143   garnet-sillimanite-biotite (Grt-Sil-Bt) gneiss, hornblende-biotite gneiss, marble and skarns, pyroxene

144   granulite, and orthopyroxene-bearing amphibolite (Fig. 1c; Shiraishi et al., 1997). Previous SHRIMP

145   U-Pb zircon dating of a Sil-Grt-Bt gneiss from Perlebandet gave an inherited core age of 1009 ± 13

146   Ma, and rim ages of 736 ± 13 Ma, 609 ± 11 Ma, and 565 ± 7 Ma (Shiraishi et al., 2008). Among the

147   three rim ages, the latter two are considered as metamorphic, whereas the detrital or metamorphic

148   origin of the first one remains unclear (Shiraishi et al., 2008). Sillimanite is the most common

149   aluminosilicate mineral, and retrograde andalusite and kyanite are locally present (Kawakami et al.,

150   2010). Otsuji et al. (2013) reported low Sr and oxygen isotope ratios from Perlebandet

151   metacarbonates, which are not characteristic of continental settings. These low Sr isotope ratios can be

152   attributed to interaction with low Sr-bearing magmatic fluids or to the older depositional age of

153   Perlebandet metacarbonates compared to that from other parts of the SRM (Otsuji et al., 2013). Otsuji

154   et al. (2016) further pointed out that Nd and Sr isotopic data from metacarbonate rocks from

155   Perlebandet neither match the data from the rocks in the SW terrane, nor from the Balchenfjella in the

156   NE terrane. Based on these data, they proposed that Perlebandet carbonates were deposited in an

157   environment surrounding an isolated seamount in the Tonian to Cryogenian period, and that

158   amalgamation of Gondwana and the final closure of Mozambique Ocean and East Antarctic Ocean

159   took place at ca. 660-550 Ma (Otsuji et al., 2016).

160

161   **Analytical methods**

162   Quantitative analysis of rock-forming minerals and X-ray elemental mapping of thin section

163   samples were performed by a JEOL JXA-8105 superprobe. Analytical conditions for quantitative

164   analyses except for apatite were 15.0 kV acceleration voltage, 10 nA beam current, and 3 μm beam

165   diameter. The counting time for the peak and backgrounds was 30 s and 15 s for Cl, 60 s and 30 s for F,

166   and 10 s and 5 s for other elements. Analytical conditions for quantitative analysis of apatite followed

167   that recommended by Goldoff et al (2012). Natural and synthetic minerals (Astimex MINM25-53)

168   were used as standards and ZAF correction was applied. Analytical conditions for X-ray elemental

169   mappings were acceleration voltage of 15.0 kV, probe current of 50 nA, focused beam to 3 μm beam

170   diameter, and dwell time of 25-40 milliseconds. Electron microprobe analysis of rutile was also done

171   by a JEOL JXA-8105 superprobe, following analytical conditions recommended by Zack et al. (2004).

172   Cathodoluminescence (CL) images were obtained using a JEOL JXA-8105 superprobe equipped

173   with Hamamatsu Photonics high voltage power supply C9525 and photon counting unit C9744.

174   Analytical conditions for CL mapping were 15.0 kV acceleration voltage, 1 nA beam current, focused

175   beam to 10 μm beam diameter, and dwell time of 1 msec.

176   Minerals were also qualitatively identified by a Hitachi S3500H scanning electron microscope

177   equipped with an EDAX X-ray analytical system. Laser Raman spectroscopy (JASCO NRS 3100)

178   was used to identify Al_2SiO_5 minerals.

179   *In situ* zircon U-Pb dating on thin section samples via LA-ICP-MS was carried out using a Nu

180   Plasma II HR-MC-ICPMS coupled to a NWR femtosecond laser-ablation system. Backscattered

181   electron (BSE) and CL images were obtained prior to the analyses to identify spot positions,

182   overlapping multiple growth zones, grain edges, cracks or damaged zircon grains. Detailed analytical

183   conditions of the LA-ICP-MS analysis are given in Higashino et al. (2015a). Data were processed and

184   plotted using *Isoplot 4.15* (Ludwig, 2012). All of the above analyses were done at the Department of

185   Geology and Mineralogy, Graduate School of Science, Kyoto University.

186

187   **Sample localities and sample descriptions**

188   The samples used in this study are two Grt-Bt gneisses [samplesTK2009113001B (3001B) and

189   TK2009112601C (2601C)] and three Grt-Sil-Bt gneisses [samples TK2009113001G (3001G),

190   TK2009113001H (3001H) and TK2009112602D (2602D)] collected during the summer season of the

191   51st Japan Antarctic Research Expedition (JARE51; Tsuchiya et al., 2012). Samples were collected

192   from the northern half of Perlebandet (Fig. 1c). The common Al_2SiO_5 mineral in these gneisses is

193   sillimanite, found as inclusions in cores of garnet and as a matrix mineral defining the gneissose

194   structure (Fig. 2a-d). A rare sample with strong retrogression (sample 3001G) contains secondary

195   andalusite, kyanite, and sillimanite replacing garnet (Fig. 2e-n). Detailed descriptions of the samples

196   studied are given below, and representative mineral analyses are given in Table 1.

197

198   ***Garnet-sillimanite-biotite gneiss (samples 2602D and 3001H)***

199   These gneisses consist of garnet, sillimanite, biotite, K-feldspar, quartz and plagioclase (An19-23

200   in 2602D, and An13-17 in 3001H), and subordinate rutile, ilmenite, zircon, monazite and apatite.

201   Muscovite is only present as a secondary mineral. Sillimanite is abundant in the matrix and also

202   present as inclusions in cores of garnet (X_{Mg} = 0.25-0.29 in 2602D, and X_{Mg} = 0.25-0.32 in 3001H)

203   (Fig. 2a). Biotite is not included in garnet. Garnet is replaced by secondary biotite at the rim and along

204   the cracks. It does not preserve chemical zoning, except for the rims and along the cracks affected by

205   the retrograde re-equilibration. The highest X_{Mg} content of garnet is preserved distant from the cracks

206   where the retrograde effects are minimal. In both samples, sillimanite and biotite partly replace garnet

207   rim. Retrograde biotite tends to have lower TiO_2 contents compared to matrix biotite. Cracks in garnet

208   are filled with retrograde biotite with the lowest Cl (Cl ~ 0.01 wt.%) and the lowest TiO_2 (< 0.29 wt.%)

209   contents.

210   In sample 2602D, garnet rim contain inclusions of quartz and K-feldspar. Matrix biotite has

211   moderate Cl content (0.17-0.22 wt.%, X_{Mg} = 0.41-0.51) and the highest TiO_2 content (2.04-3.96

212   wt.%). Retrograde biotite (Cl < 0.15 wt.%, TiO_2 = 0.98-2.82 wt.%, X_{Mg} = 0.45-0.48) and plagioclase

213   (An18-23) replace garnet at the rim (X_{Mg} = 0.11-0.13). Matrix sillimanite very rarely includes garnet

214   (X_{Mg} = 0.23-0.24). Rutile in the matrix and that included in sillimanite gave Zr contents of 1125-1466

215   ppm (average = 1359 ppm; 8 points) and 1917-1947 ppm, respectively.

216   In sample 3001H, some sillimanite grains contain inclusions of green spinel. Biotite in this

217   sample has very low Cl content (Cl < 0.03 wt.%, X_{Mg} = 0.42-0.49) irrespective of its mode of

218   occurrence. Garnet is replaced by biotite (Cl < 0.02 wt.%) and plagioclase (An16-18) at the rim (X_{Mg} =

219   0.10-0.12). Matrix sillimanite rarely includes rutile (Zr = 1473-1636 ppm). Rutile in the matrix has a

220   Zr content of 1125-2162 ppm (average = 1712 ppm; 15 points).

221

222   ***Strongly retrogressed garnet-sillimanite-biotite gneiss (sample 3001G)***

223   This is a folded, pelitic gneiss with sillimanite porphyroblasts (ca. 1cm in length). The matrix of

224   this gneiss mainly consists of biotite, garnet, sillimanite, K-feldspar, plagioclase (An26-31), quartz

225   and retrograde andalusite, kyanite, sillimanite and muscovite (Fig. 2b-n). K-feldspar is especially

226   abundant in the matrix (Fig. 2e-f). Accessory minerals are ilmenite, zircon, monazite and rare rutile.

227   Ti-oxide minerals are mostly ilmenite in the matrix, but rare rutile (Zr = 874-1273 ppm; average of 15

228   points = 1139 ppm) is preserved as inclusions in garnet (Fig. 2o) and in K-feldspar. Myrmekite is also

229   present in the matrix. Garnet in this sample is strongly replaced mainly by biotite, plagioclase,

230   andalusite, kyanite, and sillimanite (Fig. 2e-n).

231   Sillimanite is the only Al_2SiO_5 mineral included in garnet. Prismatic sillimanite porphyroblast in

232   the matrix has an inclusion-poor core and inclusion-rich rim (Fig. 2b, c). Sillimanite porphyroblasts up

233   to 1 cm in diameter show numerous subgrains and often includes smaller prismatic sillimanite with

234   crystallographic orientations different from that of the host sillimanite (Fig. 2c). The core of

235   sillimanite porphyroblast includes plagioclase (An33-37), K-feldspar and moderately Cl-bearing

236   biotite (0.17-0.30 wt.%; Table 1). The rim of sillimanite can be recognized by the presence of

237   abundant inclusions of Zn-bearing spinel (ZnO = 4-6 wt.%, X_{Mg} [= Mg/(Mg+Fe$_{total}$)] = 0.18-0.22),

238   plagioclase (An31-35), garnet (X_{Mg} = 0.18-0.19), biotite (Cl < 0.32 wt.%), ilmenite, and rare quartz

239   (Fig. 2c, d). Sillimanite that is replacing garnet (Fig. 2e, i, j) commonly includes Zn-bearing spinel

240   crystals, resembling the rim of prismatic sillimanite in the matrix. Randomly-oriented, fibrolitic

241   sillimanite is locally formed along the grain boundaries of matrix minerals.

242   Garnet is mostly xenomorphic, and includes sillimanite, Zn-bearing spinel, biotite, plagioclase,

243   quartz, ilmenite and zircon (Fig. 2k-n). It is replaced by retrograde minerals such as biotite, andalusite,

244   kyanite, sillimanite, muscovite, plagioclase and quartz (Fig. 2f-n). Replacement by biotite +

245   plagioclase intergrowths is also common (Fig. 2i-j). Garnet that locally includes Zn-bearing spinel

246   overgrows sillimanite porphyroblasts (Fig. 2b-d). Spinel included in such garnet is more Zn-rich than

247   that included in sillimanite. Garnet that overgrows sillimanite and separate garnet grains in the matrix

248   both show decreasing X_{Mg} from the core (X_{Mg} = 0.15-0.21) to the rim (X_{Mg} = 0.10-0.14). The X_{Ca} [=

249   Ca/(Fe+Mn+Mg+Ca)] slightly decreases towards the rim or remains constant at 0.04-0.07 (Table 1).

250   These garnet zonings are diffuse and are strongly affected by retrograde re-equilibration.

251   Biotite included in garnet-overgrowth on sillimanite (Fig. 2b) shows high Cl (< 0.41wt.% Cl) and

252   X_{Mg} (~ 0.63) and varying TiO$_2$ (2.3-6.0 wt.%) (Fig. 3a, b). Biotite included in sillimanite

253 porphyroblast shows moderate Cl contents (0.17-0.30 wt.%) with high X_{Mg} (0.46-0.56) and varying

254 TiO$_2$ (2.8-5.0 wt.%) (Fig. 3a, b). Matrix biotite shows moderate Cl contents (0.13-0.25 wt.%) with

255 lower X_{Mg} ($\sim$ 0.40) and moderate TiO$_2$ (2.5-3.6 wt.%) (Fig. 3a, b). Biotite in the biotite-plagioclase

256 intergrowth replacing garnet (Fig. 2g, i) shows moderate TiO$_2$ (3.2-4.2 wt.%) and Cl (0.17-0.24 wt.%)

257 contents and X_{Mg} ($\sim$ 0.47) value (Fig. 3a, b). Apparently retrograde, crack-filling biotite in garnet (Fig.

258 2k-n) shows moderate to low Cl (0.09-0.16 wt.%) and low TiO$_2$ (1.9-2.5 wt.%) contents (Fig. 3a, b).

259 Retrograde biotite developed at garnet rims also shows similar compositions to the crack-filling biotite

260 (Fig. 3a, b). There is a clear tendency for prograde biotites, such as inclusions in garnet and sillimanite

261 and some of the matrix biotite, to show Cl-rich composition and higher TiO$_2$ and X_{Mg} values than the

262 retrograde ones.

263 Andalusite intergrown with biotite commonly replaces garnet (Fig. 2f-e). Retrograde andalusite

264 is commonly accompanied by sillimanite and rare kyanite (Fig. 2e-n). Garnet is Fe-richer around the

265 andalusite-bearing replacement, and andalusite in the replacement locally includes irregularly-shaped

266 garnet and/or Zn-bearing spinel (Fig. 2k-n). Andalusite is never found as inclusions in garnet, and is in

267 contact with the matrix phases even when it is surrounded by garnet (Fig. 2k-n).

268 Kyanite is rare, and tends to be finer-grained than other Al$_2$SiO$_5$ polymorphs and is never found

269 as inclusions in garnet. It replaces garnet together with biotite, andalusite and sillimanite (Fig. 2g-j, m,

270 n). The CL images combined with laser Raman spectroscopy are useful in identifying dispersed

271 fine-grained kyanite because kyanite is more luminescent than sillimanite (moderately bright) and

272 andalusite (dark) (Fig. 2g-j). Zn-bearing spinel is also found as inclusions in some kyanite grains.

273 The composition of Zn-bearing spinel included in all Al_2SiO_5 polymorphs and garnet varies from

274 ZnO = 4.0-5.0 wt.% and X_{Mg} = 0.28 to ZnO = 11-13 wt.% and X_{Mg} = 0.18.

275

276 ***Garnet-biotite gneiss (sample 3001B)***

277 This gneiss mainly consists of garnet, biotite, quartz, plagioclase and K-feldspar, with accessory

278 zircon, ilmenite, fluorapatite and minor sulfide (Fig. 4a-c). Myrmekite is present in the matrix. Biotite

279 included in garnet (Fig. 4a-c) shows high TiO_2 (3.5-7.3 wt.%) and moderate Cl (mostly 0.20-0.34

280 wt.%) contents and high X_{Mg} (~ 0.6) (Fig. 3c, d). Biotite in the matrix (Fig. 4a-c) has moderate TiO_2

281 (3.3-4.5 wt.%) and Cl (0.11-0.25 wt.%) contents and X_{Mg} of ~ 0.4 (Fig. 3c, d; Table 1). Retrograde

282 biotite next to garnet, and crack-filling biotite in garnet (Fig. 4a-c) both show lower Cl contents below

283 0.21 wt.% (Fig. 3c, d). Some of the matrix biotite and retrograde biotites (in biotite-plagioclase

284 intergrowths and retrograde biotite next to garnet) share the same chemical characteristics of having

285 low TiO_2 and Cl contents and low X_{Mg} (Fig. 3c, d).

286

287 ***Garnet-biotite gneiss (sample 2601C)***

288 This gneiss mainly consists of garnet, biotite, K-feldspar, quartz and plagioclase (Fig. 4d-f).

289   K-feldspar is abundant, and randomly-oriented secondary muscovite is present in the matrix.

290   Accessory minerals are zircon, ilmenite and fluorapatite. Minor sulfide is included in garnet and minor

291   myrmekite is locally present in the matrix. This sample has the most Fe-rich whole-rock composition

292   among the samples studied as suggested by the Fe-rich composition of mafic minerals (X_{Mg} of biotite

293   and garnet = 0.06-0.22; Table 1). Separate biotite grains in the matrix (Fig. 4d-f) show the highest Cl

294   contents (0.61-0.68 wt.%) and the highest X_{Mg} ($\sim$ 0.2) in this sample (Figs. 3e, 3f and 4d-f). Biotite

295   replacing garnet rim as biotite-plagioclase intergrowths (Fig. 4d-f) also show high X_{Mg} ($\sim$ 0.2) and

296   moderate to high Cl content (0.32-0.41 wt.%) (Fig. 3e, f). It shares the same chemical characteristics

297   as retrograde biotite near garnet. Crack-filling biotite in garnet (Fig. 4d-f) shows the lowest X_{Mg} and Cl

298   contents (Fig. 3e, f). No systematic variation in TiO_2 content (2.2-3.8 wt.%) is observed among

299   different biotite types in this sample (Fig. 3e, f).

300

301   **LA-ICPMS U-Pb zircon dating**

302   Zircon is commonly oval-shaped, and the diameter of zircon reported below represents the length

303   of the shorter axis. Weighted mean and lower intercept ages given below are at 95% confidence level.

304   Unless specified, ages reported below refer to $^{206}Pb/^{238}U$ results. A summary of the results of

305   LA-ICPMS U-Pb zircon dating is given in Supplementary Table 2.

306

307   *Sample 3001G*

308   Zircon in the matrix is commonly shorter than 100 μm in diameter, and shows oscillatory zoning

309   (Fig. 5a-h). Analyses gave concordant U-Pb ages of ca. 1200-1100 Ma, 950-900 Ma, 750-700 Ma and

310   650-550 Ma. Ages older than 700 Ma are in most cases obtained from zircon cores, and the youngest

311   ages of ca. 580 Ma are in most cases obtained from rims. Ages older than 900 Ma tend to have high

312   Th/U ratios from 0.20 up to 1.1, while the younger age domains (750-550 Ma) give low Th/U ratios

313   below 0.20 (Figs. 5a-h and 6a; Table 2). The weighted mean U-Pb age of zircon rims from matrix

314   grains is 581 ± 10 Ma (n = 5, mean square of weighted deviates (MSWD) = 1.3, probability = 0.28).

315   Zircon included in garnet is commonly about 50 μm in diameter, and tends to have oscillatory

316   zoned cores with bright- and dark-CL zones (Th/U = 0.01-0.40, mostly around 0.25), discordantly

317   overgrown by dark-CL rims (Th/U = 0.01-0.03) (Fig. 5e, h). The lower intercept age for selected rim

318   analyses of zircon included in garnet is 578 ±   9 Ma (n = 6, MSWD = 1.3, probability = 0.28), and

319   Th/U ratios of these zircon rims with concordant ages are 0.04-0.07. Rim and mantle of a zircon grain

320   included in the inclusion-rich rim of a sillimanite porphyroblast yielded 575 ± 13 Ma (n = 2, Th/U =

321   0.04-0.09) (Fig. 5g).

322   Zircon in the garnet breakdown microstructure of Cl-poor Bt + Ms ± And shows similar zoning to

323   zircon included in garnet (Fig. 5a-d). The weighted mean U-Pb age of zircon rims (and mantles with

324   similar age) in such microstructure is 573 ± 5 Ma (n = 9, MSWD = 0.83, probability = 0.57).

325

Sample 3001B

Zircon in the matrix and zircon inclusions in garnet are commonly 30-70 μm in diameter, and shares similar microstructural features. The inherited core and mantle of zircon show oscillatory zoning under CL and BSE images, which are discordantly overgrown by relatively bright-CL rim (Figs. 5i-l, 6b). Zircon in this sample yielded concordant U-Pb ages of 850-700 Ma and 630-550 Ma (Fig. 6b). The youngest rim age from matrix zircon is 551 ± 14 Ma. Cores and rims of zircon included in garnet gave 758-585 Ma. Among them, the weighted mean of rims is 596 ± 7 Ma (n = 4, MSWD = 0.74, probability = 0.53). Both in the matrix zircon and inclusion zircon in garnet, domains of ca. 600 Ma commonly correspond to the bright-CL rim, and show high Th/U ratios up to 1.6 (Fig. 5i, j). However, some dark-CL parts with ca. 600 Ma age show relatively low Th/U ratios (0.05-0.38) (Fig. 5k).

Sample 2601C

Zircon in the matrix and included in garnet are commonly 60-100 μm and 20-70 μm in diameter, respectively (Fig. 5m-t). They share the same microstructural characteristics. The cores of zircon are oscillatory zoned and bright under CL image, or unzoned and dark (Fig. 5m-t). Several-μm to ca. 10 μm thick, bright-CL rims are commonly developed (Fig. 5m-t except for 5o). The oscillatory zoned

19

343 cores tend to give older ages (> 600 Ma) than the unzoned dark-CL ones. Zircon in the matrix and

344 inclusions in garnet both show concordant U-Pb ages of ca. 600-550 Ma (Figs. 5m-t, 6c). The

345 weighted mean U-Pb age of the rims of zircon included in garnet is 583 ± 6 Ma (n = 17, MSWD = 1.14,

346 probability = 0.31). No significant difference is observed between the age distribution patterns of

347 matrix zircon and zircon inclusions in garnet. The Th/U ratios of zircon domains with 600-550 Ma

348 ages are mostly below 0.40 (Figs. 5m-t, 6d).

349

350 **Discussion**

351 ***Pressure-temperature path of the pelitic gneiss from Perlebandet***

352   Sample 3001G is strongly affected by retrograde metamorphism as suggested from the presence

353 of retrograde andalusite and kyanite. Therefore, it is suitable for constraining the retrograde

354 metamorphic *P-T* conditions. On the other hand, samples 2602D and 3001H are less affected by

355 retrograde overprint, and thus used to estimate peak metamorphic conditions.

356

357 *1. Prograde to peak metamorphic conditions*

358   In all the sillimanite-bearing samples (3001G, 2602D and 3001H), sillimanite is commonly

359 found as porphyroblasts in the matrix, and is considered to have been stable during peak

360 metamorphism. The absence of prograde muscovite along the gneissose fabric together with the

361   presence of sillimanite + K-feldspar in the matrix suggest that peak metamorphic conditions exceeded

362   reaction (1)

363          $Ms + Ab + Qtz \rightarrow Sil + Kfs + H_2O$ or melt.   (1)
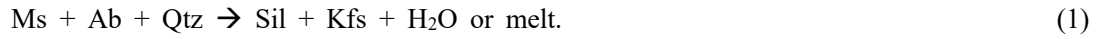
364   which was responsible for the formation of the core of sillimanite porphyroblasts in sample 3001G.

365   Sillimanite inclusions are abundant in garnet cores of samples 2602D and 3001H, and K-feldspar

366   is also abundant in the matrix. Sillimanite in the matrix of sample 3001G is partly to completely

367   overgrown by garnet (Fig. 2b-d), and some of the garnet overgrowths include Zn-bearing spinel grains

368   (Fig. 2b-d), suggesting consumption of the sillimanite rims that are hosting spinel to form garnet with

369   X_{Mg} = 0.10-0.20 (Fig. 7). Garnet with kyanite or andalusite inclusions is not seen in all studied

370   samples. These are consistent with the progress of reaction (Fig. 7)

371          $Sil + Bt + Qtz \rightarrow Grt + Kfs + $ melt.   (2)
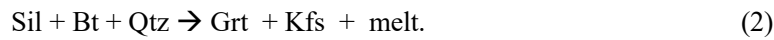
372   The absence of cordierite in all garnet-bearing felsic gneiss samples suggests that the *P-T* conditions

373   did not exceed the reaction

374          $Bt + Sil + Qtz \rightarrow Grt + Crd + Kfs + $ melt.   (3)
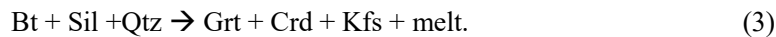
375   Garnet, plagioclase, biotite and rare quartz are included in the inclusion-rich rim of a sillimanite

376   porphyroblast in sample 3001G (Fig. 2b-d). The composition of biotite and garnet separately included

377   in sillimanite (Table 1) are most likely to preserve compositions of entrapment, because sillimanite

378   would hinder Fe-Mg exchange reactions between garnet and biotite after entrapment. Therefore,

379   prograde *P-T* conditions can be estimated using these minerals. The Grt-Bt (GB) geothermometer

380   (Holdaway et al., 1997; Holdaway, 2000) and the garnet-Al_2SiO_5-quartz-plagioclase (GASP)

381   geobarometer (Holdaway, 2001) yielded ca. 700 ºC, 0.47 GPa, which is in agreement within error of

382   the geothermobarometry ($\pm$ 50 ºC and $\pm$ 0.10 GPa) with *P-T* conditions of reaction (2) for the observed

383   garnet composition of X_{Mg}^{Grt} = 0.10-0.20 in the NaKFMASH system (Fig. 7). The rarity of quartz

384   inclusions in the sillimanite rims may imply local absence of quartz, in which case the result may

385   represent the highest-*P* estimate. Although the Grt-Bt thermometer of Holdaway (2000) does not

386   account for the effects of F and Cl, calculations using the Zhu and Sverjensky (1992) calibration

387   showed that the opposing effects of F (*T* increase) and Cl (*T* decrease) on the temperature estimate

388   canceled each other out, and thus the effects of F and Cl are negligible in this sample.

389   On the other hand, the absence of a significant low-*P* retrograde overprint in samples 2602D and

390   3001H suggests that such rocks preserve peak metamorphic conditions better. In these samples, garnet

391   core with sillimanite inclusions (Fig. 2a) and matrix plagioclase core are interpreted as coexisting with

392   sillimanite and quartz, and used in the GASP geobarometry (Holdaway, 2000). For peak temperature

393   estimate, Zr-in-rutile thermometry (Zack et al., 2004; Tomkins et al., 2007) was applied to rutile

394   included in sillimanite and that in the matrix. The Tomkins et al. (2007) calibration is preferred in this

395   study since it takes pressure effect into account and is experimentally calibrated. Peak *P-T* conditions

396   estimated by the intersection of Zr-in-rutile thermometry (Tomkins et al., 2007) and GASP

397   geobarometry (Holdaway, 2001) are ca. 768-840 °C and 0.8-1.0 GPa. The Grt-Bt geothermometry is

398   considered less reliable than the Zr-in-rutile thermometry in this case, because the X_{Mg} of matrix

399   biotite or inclusion biotite in garnet is more susceptible to retrograde re-equilibrium compared to rutile

400   included in sillimanite. The peak *P-T* conditions above are consistent with those of reaction (2) for

401   garnet with composition of $X_{Mg}^{Grt} \sim 0.40$, higher than that observed at the sillimanite-bearing garnet

402   core (Table 1; Fig. 7), implying a modification of X_{Mg} of garnet during retrograde metamorphism.

403   Sample 3001G, affected by the low-*P* retrograde overprint, also preserves rutile as inclusions in

404   garnet and K-feldspar or rarely in the matrix (Fig. 2o). The Zr-in-rutile thermometry gives temperature

405   estimates (743-780 °C assuming 1.0 GPa) almost consistent with those of samples 2602D and 3001H.

406   This observation strongly supports that sample 3001G shared the same peak *P-T* conditions as other

407   samples before the low-*P* retrograde overprint.

408

409   **2.   *Retrograde metamorphic conditions and proposed P-T path***

410   In sample 3001G, peak garnet is commonly replaced by three Al_2SiO_5 polymorphs (Fig. 2i-j, m-n).

411   It is difficult to define the sequence of andalusite and kyanite formation from their microtextures (Fig.

412   2g-j, m-n). Some sillimanite grains surrounding retrogressed garnet and including Zn-bearing spinel

413   grains in sample 3001G (Fig. 2i) may have been originally included in garnet and survived the garnet

414   breakdown reactions, because Zn-bearing spinel inclusions are the typical feature for prograde

415   sillimanite rims (Fig. 2b, c). However, the coexistence of andalusite+sillimanite, andalusite+kyanite,

416   and andalusite+kyanite+sillimanite in the replacement microtextures of garnet suggests garnet

417   breakdown near the $P\text{-}T$ conditions of the Al_2SiO_5 triple point. Since the coexistence of three Al_2SiO_5

418   polymorphs in the garnet breakdown microstructure is only preserved in sample 3001G, it is likely that

419   localized fluid infiltrated this sample at $P\text{-}T$ conditions of the Al_2SiO_5 triple point to trigger the

420   retrograde reaction. This is also supported by the GASP geobarometry (Holdaway, 2000) and the

421   Grt-Bt geothermometry (Holdaway et al., 1997; Holdaway, 2000) using mineral compositions of the

422   breakdown microstructure of garnet into biotite, plagioclase, quartz and Al_2SiO_5 minerals, which yield

423   $P\text{-}T$ conditions of ca. 600 ^{o}C and 0.48 GPa, close to the Al_2SiO_5 triple point (Fig. 7). The almost

424   complete cancelation of the opposite effects of F and Cl in biotite on the Grt-Bt geothermometer is

425   confirmed by using Zhu and Sverjensky (1992) calibration, supporting the above $P\text{-}T$ estimate. Since

426   prograde (ca. 700 ^{o}C, 0.47 GPa) and retrograde (ca. 600 ^{o}C, 0.48 GPa) $P\text{-}T$ conditions are estimated

427   using the same geothermobarometers, and since the effects of F and Cl in biotite can be ignored, we

428   consider the differences between them meaningful. Therefore, by connecting prograde, peak and

429   retrograde $P\text{-}T$ estimates from three samples, a counterclockwise $P\text{-}T$ path for the Perlebandet rocks is

430   proposed (Fig. 7).

431   Garnet rims are also locally replaced by the intergrowth of biotite and plagioclase in all samples.

432   Utilizing the composition of garnet rims and biotite and plagioclase in the intergrowth, and applying

433   the Grt-Bt geothermometer (Holdaway et al., 1997; Holdaway, 2000) and the

434   garnet-biotite-plagioclase-quartz (GBPQ) geobarometer (Wu et al., 2004), retrograde *P-T* conditions

435   of garnet breakdown to biotite + plagioclase are estimated. These vary depending on samples, and are

436   ca. 580 $^{\circ}$C and ca. 0.40 GPa for sample 3001G (average of 4 estimates; Fig. 7), ca. 640 $^{\circ}$C, 0.66 GPa

437   for sample 3001B (average of 5 estimates; Fig. 7), and ca. 760 $^{\circ}$C, ca. 0.97 GPa for sample 2601C

438   (average of 5 estimates; Fig. 7). Among these, an estimate from sample 3001G is consistent with the

439   estimate by the GB-GASP pair (Fig. 7). These *P-T* conditions are consistent with the proposed

440   counterclockwise *P-T* path (Fig. 7).

441   This proposed *P-T* path is very similar to that estimated for Brattnipene, central SRM (Fig. 1b;

442   e.g., Adachi et al., 2013; Baba et al., 2013), suggesting that Perlebandet belongs to the SW terrane of

443   the SRM (Fig. 1b; e.g., Mieth et al., 2014). Our results of zircon dating (Fig. 6) are consistent with

444   previous results from Perlebandet (Shiraishi et al.. 2008) in that detrital ages older than 1200 Ma are

445   absent. This is also true for SW terrane rocks of the SRM (Osanai et al., 2013), and thus zircon data

446   also support Perlebandet as being part of the SW terrane (Fig. 1b).

447

448   ***Timings of Cl-bearing fluid infiltration and relationship with partial melting***

449   The presence of Cl-rich biotite has been considered as evidence for the presence of brines (e.g.,

450   Newton et al., 1998; Manning and Aranovich, 2014; Safonov et al. 2014). Although the $f(H_2O)/f(HCl)$

451   ratio of the coexisting fluid can be deduced from the composition of biotite and apatite (e.g., Selby and

452   Nesbitt, 2000), it should be noted that the salinity of the fluid cannot be directly determined by this

453   method (e.g., Rubenach, 2005). However, if the fluid coexists with silicate melt, the HCl concentration

454   can be related to the total Cl concentration in the fluid by the equation $\log(HCl/\Sigma Cl)^{aq} =$

455   -0.63-0.00035*P (bars) up to 0.67 GPa (Piccoli and Candela, 1994). This means that at pressures

456   typical of the middle crust, most of the Cl forms complexes with cations other than H. Therefore,

457   considering a case where Cl-bearing fluid coexists with melt, low $f(H_2O)/f(HCl)$ ratios in the fluid

458   indicates abundant chloride salts in the fluid (i.e., high salinity). It is important, therefore, to carefully

459   consider the melt-related processes that can increase Cl contents in biotite in addition to fluid-related

460   processes. Several possible mechanisms to elevate Cl-contents in biotite are listed below, and their

461   likeliness is discussed:

462   (a) Original Cl-rich whole-rock compositions allowed biotite to become Cl-rich.

463   (b) Consumption of originally Cl-bearing biotite through melting reactions caused an increase

464   of Cl-content in remaining biotite.

465   (c) Retrograde consumption of H_2O by hydration reactions increased Cl content in the fluid,

466   resulting in the increase of Cl in coexisting biotite (Kullerud, 1996; Markl and Bucher,

467   1998).

468   (d) Subsolidus Cl-rich fluid infiltration occurred (e.g., Newton et al., 1998; 2014; Higashino et

469   al., 2015b).

470   (e) Infiltration of Cl-rich fluid triggered anatexis, and preferential partitioning of H_2O into the

471   melt resulted in enrichment of Cl in the fluid (e.g., Aranovich et al., 2013; Safonov et al.,

472   2014).

473   Cases (a)-(c) assume closed system behavior of Cl, and (d)-(e) assume open system behavior of Cl.

474   Case (b) plays an important role if the partition coefficient of Cl between granitic melt and biotite is

475   greater than 1. Based on experiments at 0.2 GPa, D_{Cl}(biotite/melt) is estimated to be ~1 to 6

476   (Icenhower and London, 1997). Recently, Safonov et al. (2014) performed a melting experiment of a

477   biotite-amphibole gneiss with H_2O-CO_2-(K, Na)Cl fluids at 0.55 GPa and 750-800 °C. Their

478   compositional data of coexisting biotite (X_{Mg} = 0.43-0.57) and melt imply that Cl is preferentially

479   incorporated in the melt rather than in biotite, that is, D_{Cl}(biotite/melt) is less than 1 at 0.55 GPa and

480   800 °C. Therefore, the behavior of Cl under middle crustal depths can be different from that in shallow

481   levels of the crust, and if this is the case, case (b) alone is not likely a strong process to elevate Cl

482   content in biotite, at least for samples 3001B and 3001G having X_{Mg} values of biotite (X_{Mg} =

483   0.40-0.64; Table 1) similar to the experiment of Safonov et al (2014).

484   Sample 3001G preserves Cl-rich biotite (~ 0.4 wt.%) as inclusions in garnet. Biotite inclusions in

485   garnet tend to re-equilibrate and change X_{Mg} on cooling, while preserving their original halogen

486   content. Biotite was already Cl-rich prior to the garnet-formation by reaction (2), because moderately

487   Cl-bearing biotite (< 0.30 wt.%Cl) is included in sillimanite porphyroblasts predating garnet

488   formation (Fig. 3a). Biotite inclusions in garnet from sample 3001B show the highest Cl-content in the

489   sample, suggesting prograde formation of Cl-enriched biotite (Fig. 3b). Therefore, case (c) can be

490   ruled out. Although case (a) cannot be ruled out, we consider that the similar timing of Cl-enriched

491   biotite formation in different lithologies can be best explained by the infiltration of a Cl-rich fluid. The

492    $\log[f(H_2O)/f(HCl)]$ and $\log[f(H_2O)/f(HF)]$ values of the fluid estimated assuming its presence during

493   prograde stage for these two samples are in good agreement (Table 1), supporting the infiltration of

494   fluids with a similar composition. External input of Cl-rich fluid is also supported by the localized

495   field distribution of Cl-rich minerals in the SRM as discussed in the next section.

496   At P-T conditions estimated for reaction (2) in Perlebandet (~700 °C and ~0.5 GPa), aH$_2$O of a

497   pelitic gneiss undergoing partial melting can be estimated to be ~ 0.85 (Clemens and Vielzeuf, 1987).

498   Ascribing this lowering of aH$_2$O to the addition of NaCl and KCl, XH$_2$O is estimated to be ~ 0.9

499   using the aH$_2$O-XH$_2$O relationship by Aranovich and Newton (1997), corresponding to ~ 26 wt%

500   NaCl (KCl). This is the highest estimate of salinity of the fluid, because CO$_2$ can also contribute to

501   lower aH$_2$O. It is difficult, however, to envisage source of the voluminous high-salinity fluid. More

502   likely case is an infiltration of smaller volume of lower salinity fluids that continually increased

503   salinity through preferential partitioning of H$_2$O into anatectic melts (Aranovich et al., 2013). In such

504   case, we may assume that the fluid-present reaction such as follows (e.g., Yardley and Barber, 1991)

505   took place prior to the dehydration melting reaction (2),

506   Bt + Sil + Kfs + Qtz + H_2O → melt   (4).
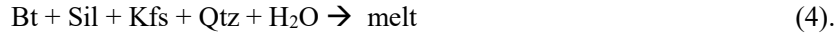
507   As fluid-present melting reaction proceeds by consuming H_2O, $\log[f(H_2O)/f(HCl)]$ and

508     $\log[f(H_2O)/f(HF)]$ values of the fluid will decrease, resulting in an increase of Cl content in biotite.

509   Small volume of the fluid will be soon used up, resulting in cessation of the fluid-present partial

510   melting reactions, and further melting must proceed by dehydration melting reactions (e.g., Brown,

511   2013) such as reaction (2) in the present case. The escape of concentrated fluids from the system with

512   the assistance of deformation or low wetting angle of brines will also help switching the reaction

513   from fluid-fluxed melting to dehydration melting. This process might explain why the Cl content of

514   biotite included in peritectic garnet formed by dehydration melting reaction (2) is higher than that

515   included in sillimanite porphyroblasts (Figs. 2b-d and 3).

516   On the other hand, some fluid-present melting reactions can also produce peritectic phases as

517   sillimanite and garnet (Weinberg and Hasalová, 2015). Reactions such as

518   Ms + Pl + Qtz + H_2O → Sil + Bt + melt   (5)

519   and

520   Bt $\pm$ Crd + Sil + Pl + Qtz + H_2O → Grt $\pm$ Kfs + melt   (6)
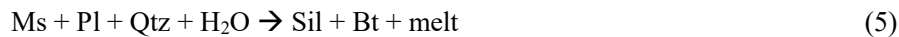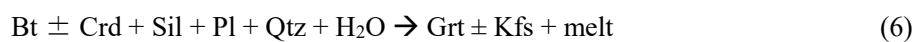
521   (Jung et al., 2000; Milord et al., 2001) are the examples reported to occur at the *P-T* conditions for the

522   beginning of partial melting in this study (~ 0.5 GPa and ~ 700 ºC). At medium pressure of ~ 0.5 GPa,

523   fluid-present melting and dehydration melting reactions take place in relatively small temperature

524   intervals. However, observed mineral compositions and sequences of reactions are mostly consistent

525   with the *P-T* diagram constructed under the scheme of dehydration melting (Fig. 7). This might

526   suggest that fluid-present melting occurred in the Perlebandet rocks only at the onset of the prograde

527   partial melting process, and the subsequent melting occurred through dehydration melting reactions.

528   In sample 3001G, matrix biotite as a remnant of reaction (2) was presumably once Cl-rich.

529   Compositional similarity between matrix biotite and microstructurally secondary biotite (Fig. 3)

530   suggests that moderately Cl-bearing matrix biotite is a result of recrystallization of former Cl-rich

531   biotite, re-equilibrated with retrograde fluids possibly released from the crystallizing melt. Using the

532   *P-T* conditions of retrograde metamorphism, $\log[f(H_2O)/f(HCl)]$ of the retrograde fluid can be

533   estimated as 4.2-4.3, with an average of 4.3 (Table 1).

534

535   ***The age of metamorphism and Cl-rich fluid infiltration***

536   In sample 3001G, rims of matrix zircon and inclusion zircon in garnet and sillimanite all yielded

537   U-Pb ages of 580-575 Ma. Most of these zircon rims show Th/U ratios below 0.1 (Fig. 6d), typical for

538   metamorphic zircon (e.g., Rubatto, 2002). The garnet-forming reaction was probably partial melting

539   reaction (2). Therefore, garnet-forming, sillimanite-grade metamorphism is likely to have occurred at

540   or after ca. 580 Ma, together with the Cl-rich fluid infiltration. Moderately Cl-bearing biotite replacing

541   garnet suggests that Cl-bearing aqueous fluid was present during retrograde garnet breakdown. The

542   weighted mean U-Pb age of rims of zircon found in the microstructure of garnet replaced by Al_2SiO_5

543   minerals and biotite is 573 ± 5 Ma. The similarity of this age with zircon rims included in garnet

544   implies that the retrogression took place soon after the peak metamorphism, or zircon was inert during

545   the retrograde breakdown of garnet.

546   Samples 3001B and 2601C both give constraints that are consistent with the above scenario. For

547   sample 3001B, the formation of garnet and moderately Cl-bearing biotite included in it (Fig. 3e, f) was

548   presumably at 596 ± 7 Ma or younger. The fluid at retrograde stage shows $\log[f(H_2O)/f(HCl)]$ value of

549   4.0-5.0, with an average of 4.5 (Table 1). For sample 2601C, garnet growth would predate or coincide

550   with 583 ± 6 Ma. Low Th/U zircon rims (Fig. 6d) supports this to be the metamorphic age. Markedly

551   high Cl concentration of isolated matrix biotite in this sample (Cl > 0.61 wt.%) reflects Mg-Cl

552   avoidance, in addition to the Cl-rich nature of the coexisted fluid, since biotite in this sample is

553   Fe-richer than other samples (Fig. 3). The $\log[f(H_2O)/f(HCl)]$ of the near-peak to retrograde fluid is

554   calculated as 3.5-4.2, with an average of 3.9 (Table 1).

555   To summarize, the timing of garnet-forming prograde metamorphism in Perlebandet is estimated

556   to be ca. 580 Ma or younger. Since biotite was already enriched in Cl before the onset of reaction (2),

557   the formation of highly to moderately Cl-bearing biotite in samples 3001G and 3001B took place

558   before or at ca. 580 Ma during prograde metamorphism. Taking into account that estimated prograde

559    $\log[f(H_2O)/f(HCl)]$ and $\log[f(H_2O)/f(HF)]$ of fluid are almost the same among the samples studied, it is

560   likely that external Cl-bearing fluid infiltration occurred, prior to or simultaneously with the

561   sillimanite-forming reaction. On the other hand, the presence of a retrograde, Cl-bearing fluid with

562    $\log[f(H_2O)/f(HCl)] = 4.0\text{-}5.0$ (with one exception of 3.5) is detected from three samples. This probably

563   lasted until ca. 550 Ma. During the retrograde decompression, $\log[f(H_2O)/f(HCl)]$ of fluids increased

564   slightly or was almost constant (Table 1; Fig. 7).

565   At the outcrop scale, fluid pathways may be localized (e.g., Aranovich et al., 2010; Dubinina et

566   al., 2015; Kusebauch et al., 2015). This is also suggested in the SRM by localized distribution of

567   post-peak Cl-rich veins in the outcrop scale in Brattnipene (Fig. 1b; Higashino et al., 2015b). The

568   localized distribution of prograde Cl-bearing biotite in Perlebandet shows that Cl-bearing fluid

569   pathways may be localized during prograde metamorphism as well, but obscured by later ductile

570   deformation.

571

572   ***Comparison with other areas of the SRM***

573   The *P-T-t* conditions of Cl-rich aqueous fluid infiltration in the SRM have been previously

574   determined from two other localities; the eastern part (Balchenfjella; Higashino et al., 2013a) and the

575   central part (Brattnipene; Higashino et al., 2015a) (Fig. 1b). In Balchenfjella, the *P-T* conditions of

576   Cl-rich biotite and apatite entrapment in the garnet rim are estimated to be ca. 800°C and 0.80 GPa at

577   603 ± 14 Ma, which corresponds to the early retrograde stage postdating a peak metamorphic event at

578   ca. 850ºC and 1.1 GPa (Higashino et al., 2013a). A subsequent Cl-poor fluid infiltration is recorded in

579   Cl-poor matrix biotite, and estimated to have occurred at 564 ± 17 Ma from the rim age of zircon in the

580   matrix (Higashino et al., 2013b). On the other hand, in Brattnipene, early retrograde Cl-rich fluid

581   infiltration is estimated at ca. 700 ºC, 0.75 GPa and after ca. 620 Ma (Higashino et al., 2015b). In

582   contrast to these post-peak Cl-rich fluid activities, the present study shows that the Cl-rich biotite

583   included in garnet was formed during prograde metamorphism possibly as a result of Cl-bearing fluid

584   infiltration. External input of Cl-rich fluid during prograde- to peak-metamorphism possibly produced

585   Cl-bearing partial melt, and its crystallization during decompression and cooling resulted in a release

586   of post-peak, Cl-bearing fluid (Fig. 7).

587   Experimental data by Safonov et al. (2014) shows that melt can contain more Cl than coexisting

588   biotite at 0.55 GPa and 750-800 ºC. The fluid released by the crystallization of such melt would have

589   significantly more Cl than coexisting melt (Webster, 1992; Aranovich et al., 2013). Therefore, one

590   possible mechanism to produce Cl-rich fluid during the retrograde stage is the crystallization of

591   Cl-bearing partial melt. However, if the partial melting and crystallization of the melt alone is the

592   cause of Cl-rich fluid, Cl-rich biotite should be more widely distributed throughout the NE terrane of

593   the SRM where partially molten granulites and migmatites are widely distributed (Fig. 1b). What is

594   actually observed in the field is the localized distribution of Cl-rich biotite and hornblende along

595   large-scale shear zones and detachments both in felsic and mafic gneisses (Fig. 1b; Higashino et al.,

596   2015a). The distribution of Cl-rich minerals corresponds with the boundaries of magnetic anomaly

597   domains of Mieth et al. (2014). This trend may be obscured by a possible granite intrusion near

598   Perlebandet that is inferred to be the source of a high-magnetic anomaly (Mieth et al., 2014), but

599   ignoring the possible effect of this granite intrusion, Perlebandet is also located along the boundaries

600   of magnetic anomaly domains which corresponds to the major tectonic boundaries (e.g., Mieth et al.

601   2014). These suggest that the input of Cl in the SRM including Perlebandet is probably external,

602   possibly as Cl-rich fluid infiltration channeled along the tectonic boundaries (e.g., Glassley et al.,

603   2010) during prograde metamorphism. One occurrence of Cl-rich biotite in Brattnipene is at a major

604   shear zone containing peridotite and pyroxenite lenses (Fig. 1b; location 4 of Higashino et al. 2013),

605   supporting this idea. Because Perlebandet and Brattnipene share the counterclockwise *P-T* paths, they

606   should both belong to the footwall side of the MTB based on the tectonic model by Osanai et al. (2013)

607   (Fig. 8). Therefore, the Cl-rich fluid infiltration presumably took place at the uppermost part of the

608   footwall of the MTB (Fig. 8).

609   Based on this tectonic constraint, there are several candidates for the origin of the Cl-rich fluids.

610   Because the Mozambique Ocean is considered to have been located between the NE and SW terranes

611   of the SRM before collision (Otsuji et al., 2016), sea water introduced into the depth and fluids

612   released from the mantle are the likely candidates, and should be examined in future studies. High Cl

613 content in biotite, hornblende and apatite is a measure of low $\log[f(H_2O)/f(HCl)]$ of fluids, implying

614 that the origin of Cl-rich fluids in the SRM can be also related to the magmatic activity during

615 collision.

616   Multiple episodes of zircon growth within single orthogneissic samples from the NE terrane with

617 ages from ca. 630 Ma to ca. 535 Ma described by Grantham et al. (2013) and the result of this study

618 from the SW terrane indicate a long history of metamorphism, magmatism and deformation that

619 affected both terranes (e.g., Elburg et al., 2016), and multiple Cl-rich fluid infiltrations took place in

620 the SRM during this period (e.g., Higashino et al., 2013; 2015a).

621

622 **Conclusion**

623   Chlorine-rich fluid infiltration into the upper-amphibolite- to granulite-facies middle continental

624 crust at the prograde stage of counterclockwise *P-T* path is likely at Perlebandet (western SRM, East

625 Antarctica). This presumably occurred in the uppermost part of the footwall of the continental

626 collision boundary at ca. 580 Ma. The localized distribution of Cl-rich biotite and hornblende along

627 large-scale shear zones and detachments in the SRM supports the external input of Cl-rich fluids

628 through tectonic boundaries during continental collision.

629

630 **Acknowledgements**

640   **References**

641   Adachi, T., Hokada, T., Osanai, Y., Nakano, N., Baba, S., Toyoshima, T., 2013. Contrasting

642   metamorphic records and their implications for tectonic process in the central Sør Rondane

643   Mountains, eastern Dronning Maud Land, East Antarctica. In: Harley SL, Fitzsimons LCW,

644   Zhao Y (ed) Antarctica and Supercontinent Evolution. Geological Society, London, Special

645   Publication 383, 113-133.

646   Aranovich, L.Y., Shmulovich, K.I., Fedkin, V.V., 1987. The H_2O and CO_2 regime in regional

647   metamorphism. International Geology Review 29, 1379-1401.

648   Aranovich, L.Y., Dubinina, E.O., Avdeenko, A.S., Lebedeva, Y.M., Bushmin, S.A.,

649   Dolivo-Dobrovol'skii, D.D., 2010. Oxygen isotopic composition of coexisting minerals of

650   sillimanite-hypersthene rocks from the Por'ya bay area: Evidence of fluid involvement in

651   granulite-facies metamorphism. Geochemistry International 48, 739-751.

652 Aranovich, L.Y., Newton, R.C., Manning, C.E., 2013. Brine-assisted anatexis: Experimental melting

653   in the system haplogranite–H_2O–NaCl–KCl at deep-crustal conditions. Earth and Planetary

654   Science Letters 374, 111-120.

655 Asami, M., Shiraishi, K., 1987. Kyanite from the western part of the Sør Rondane Mountains, East

656   Antarctica. Proceedings of the NIPR symposium on Antarctic Geosciences 1, 150-168.

657 Asami, M., Osanai, Y., Shiraishi, K., Makimoto, H., 1992. Metamorphic evolution of the Sør Rondane

658   Mountains, East Antarctica. In: Yoshida, Y., Kaminuma, K., Shiraishi, K. (Eds.), Recent

659   Progress in Antarctic Earth Science. Terra Scientific Publishing Company, Tokyo, pp. 7–15.

660 Baba, S., Osanai, Y., Nakano, N., Owada, M., Hokada, T., Horie, K., Adachi, T., Toyoshima, T., 2013.

661   Counterclockwise P–T path and isobaric cooling of metapelites from Brattnipene, Sør Rondane

662   Mountains, East Antarctica: Implications for a tectonothermal event at the proto-Gondwana

663   margin. Precambrian Research 234, 210–228.

664 Brown, M., 2013. Granite: From genesis to emplacement. GSA Bulletin 125, 1079–1113.

665 Dubinina E.O., Aranovich, L.Y., van Reenen, D.D., Avdeenko, A.S., Varlamov, D.A., Shaposhnikov,

666   V.V., Kurdyukov, E.B., 2015. Involvement of fluids in the metamorphic processes within

667   different zones of the Southern Marginal Zone of the Limpopo complex, South Africa: An

668   oxygen isotope perspective. Precambrian Research 256, 48-61.

669 Elburg, M.A., Andersen, T., Jacobs, J., Läufer, A., Ruppel, A., Krohne, N., Damaske, D., 2016. One

670   Hundred Fifty Million Years of Intrusive Activity in the Sør Rondane Mountains (East

671   Antarctica): Implications for Gondwana Assembly. The Journal of Geology 124, 1-26.

672 Glassley, W.E., Korstgårda, J.A., Sørensen, K., 2010. K-rich brine and chemical modification of the

673   crust during continent–continent collision, Nagssugtoqidian Orogen, West Greenland.

674   Precambrian Research 180, 47–62.

675 Goldoff, B., Webster, J.D., Harlov, D.E., 2012. Characterization of fluor-chlorapatites by electron

676   probe microanalysis with a focus on time-dependent intensity variation of halogens. American

677   Mineralogist 97, 1103-1115.

678 Grantham, G.H., Macey, P.H., Ingram, B.A., Roberts, M.P. Armstrong, R.A., Hokada, T., Shiraishi,

679   K., Jackson, C., Bisnath A., Manhica V., 2008. Terrane correlation between Antarctica,

680   Mozambique and Sri Lanka; comparisons of geochronology, lithology, structure and

681   metamorphism and possible implications for the geology of southern Africa and

682   Antarctica..Geological Society, London, Special Publications 308, 91-119.

683 Grantham, G.H., Macey, P.H., Horie, K., Kawakami, T., Ishikawa, M., Satish-Kumar, M., Tsuchiya,

684   N., Graser, P., Azevedo, S., 2013. Comparison of the metamorphic history of the Monapo

685   Complex, northern Mozambique and Balchenfjella and Austhameren areas Sør Rondane,

686   Antarctica: Implications for the Kuunga Orogeny and the amalgamation of N and S.

687   Gondwana. Precambrian Research 234, 85–135.

688 Grew, E.S., Asami, M., Makimoto, H., 1989. Preliminary petrological studies of the metamorphic

689   rocks of the eastern Sør Rondane Mountains. Proceedings of the NIPR symposium on Antarctic

690   Geosciences 3, 100-127.

691 Harlov, D.E., Förster, H.J., 2002. High-grade fluid metasomatism on both a local and a regional scale:

692   the Seward Peninsula, Alaska, and the Val Strona di Omegna, Ivrea-Verbano Zone, northern

693   Italy. Part 1: Petrography and silicate mineral chemistry. Journal of Petrology 43, 769-799.

694 Heinrich, W., 2007. Fluid immiscibility in metamorphic rocks. Fluid-fluid interactions. Reviews in

695   Mineralogy and Geochemistry 65, 389-430.

696 Higashino, F., Kawakami, T., Satish-Kumar, M., Ishikawa, M., Maki, K., Tsuchiya, N., Grantham,

697   G.H., Hirata, T., 2013a. Chlorine-rich fluid or melt activity during granulite facies

698   metamorphism in the Late Proterozoic to Cambrian continental collision zone- An example

699   from the Sør Rondane Mountains, East Antarctica. Precambrian Research 234, 229-246.

700 Higashino, F., Kawakami, T., Satish-Kumar, M., Ishikawa, M., Tsuchiya, N., Grantham, G.H., 2013b.

701   Multi-stage Cl-rich fluid activity and behavior of REE-bearing minerals in a Neoproterozoic

702   granulite terrane. Goldschmidt 2013 abstract, Mineralogical Magazine 77, 1298.

703   Higashino, F., Kawakami, T., Tsuchiya, N., Satish-Kumar, M., Ishikawa, M., Grantham, G.H., Sakata,

704   S., Hattori, K., Hirata, T., 2015a. Geochemical behavior of zirconium during Cl-rich aqueous

705   fluid infiltration under upper amphibolite facies metamorphism – A case study from

706   Brattnipene, Sør Rondane Mountains, East Antarctica. Journal of Mineralogical and

707   Petrological Sciences 110, 166-178.

708   Higashino, F., Kawakami, T., Tsuchiya, N., Satish-Kumar, M., Ishikawa, M., Grantham, G.H., 2015b.

709   Mass transfer in mafic gneiss during upper-amphibolite facies chloride brine infiltration.

710   Goldschmidt 2015 abstract, 1268.

711   Hiroi Y., Yanagi A., Kato M., Kobayashi T., Prame B., Hokada T., Satish-Kumar M., Ishikawa M.,

712   Adachi, T., Osanai Y., Motoyoshi Y., Shiraishi GK., 2014. Supercooled melt inclusions in

713   lower-crustal granulites as a consequence of rapid exhumation by channel flow. Gondwana

714   Research 25, 226–234.

715   Holdaway, M.J., 2000. Application of new experimental and garnet Margules data to the garnet–

716   biotite geothermometer. American Mineralogist 85, 881–892.

717   Holdaway, M.J., 2001. Recalibration of the GASP geobarometer in light of recent garnet and

718   plagioclase activity models and versions of the garnet-biotite geothermometer. American

719   Mineralogist 86, 1117-1129.

720   Holdaway, M.J., Mukhopadhyay, B., Dyar, M.D., Guidotti, C.V., Dutrow, B.L., 1997. Garnet-biotite

721   geothermometry revised: New Margules parameters and a natural specimen data set from

722   Maine. American Mineralogist 82, 582-595.

723   Holness, M.B., 1997. Surface chemical controls on pore-fluid connectivity in texturally equilibrated

724   materials. In: Jamtveit, B., Yardley, B.W.D. (Eds.), Fluid Flow and Transport in Rocks.

725   Chapman and Hall, London, pp. 149–169.

726   Holness, M.B., Cesare, B., Sawyer, E.W., 2011. Melted rocks under the microscope: Microstructures

727   and their interpretation. Elements 7, 247–252.

728   Ishikawa, M., Kawakami, T., Satish-Kumar, M., Grantham, G.H., Hokazono, Y., Saso, M., Tsuchiya,

729   N., 2013. Late Neoproterozoic extensional detachment in eastern Sør Rondane Mountains, East

730   Antarctica: Implications for the collapse of East African Antarctic Orogen. Precambrian

731   Research 234, 247-256.

732   Icenhower, J., London, D., 1997. Partitioning of fluorine and chlorine between biotite and granitic

733   melt: experimental calibration at 200 MPa H_2O. Contributions to Mineralogy and Petrology

734   127, 17-29.

735   Jacobs, J., Bauer, W., Fanning, C.M., 2003. Late Neoproterozoic/Early Palaeozoic events in central

736   Dronning Maud Land and significance for the southern extension of the East African Orogen

737   into East Antarctica. Precambrian Research 126, 27-53.

738   Jacobs, J., Elburg, M., Läufer, A., Kleinhanns, I.C., Henjes-Kunst, F., Estrada, S., Ruppel, A.S.,

739   Damaske, D., Montero, P., Bea, F., 2015. Two distinct Late Mesoproterozoic/Early

740   Neoproterozoic basement provinces in central/eastern Dronning Maud Land, East Antarctica:

741   The missing link, 15–21°. Precambrian Research 265, 249-272.

742   Jung, S., Hoernes, S., Mezger, K., 2000. Geochronology and petrology of migmatites from the

743   Proterozoic Damara Belt — importance of episodic fluid-present disequilibrium melting and

744   consequences for granite petrology. Lithos 51, 153–179.

745   Kamei A., Horie K., Owada M., Yuhara M., Nakano N., Osanai Y., Adachi T., Hara Y., Terao M.,

746   Teuchi S., Shimura T., Tsukada K., Hokada T., Iwata C., Shiraishi K., Ishizuka H., Takahashi Y.,

747   2013. Late Proterozoic juvenile arc metatonalite and adakitic intrusions in the Sør Rondane

748   Mountains, Eastern Dronning Maud Land, Antarctica. Precambrian Research 234, 47-62.

749   Kawakami, T., Hokada, T., Sakata, S., Hirata, T., 2016. Possible polymetamorphism indicated by

750   monazite and zircon dating and isotope mapping of garnet, and significance of Cl-rich biotite

751   coexisted with melt in the garnet-sillimanite gneiss, Skallevikshalsen, Lützow-Holm Complex,

752   East Antarctica. Journal of Mineralogical and Petrological Science 111, 129-143.

753   Kawakami, T., Satish-Kumar, M., Tsuchiya, N., Ishikawa, M., Higashino, F., Grantham, G.H.,

754   Yoshida, K., 2010. Pelitic metamorphic rocks from Perlebandet and Balchenfjella, Sør Rondane

755   Mountains, East Antarctica. Abstract of the First Symposium on Polar Science. GO008.

756   Kitano, I., Osanai, Y., Nakano, N., Adachi, T., 2016. Detrital zircon provenances for metamorphic

757   rocks from southern Sør Rondane Mountains, East Antarctica: A new report of Archean to

758   Mesoproterozoic zircons. Journal of Mineralogical and Petrological Science 111, 118-128.

759   Kojima, S.,   Shiraishi, K., 1986. Note on the geology of the western part of the Sør Rondane

760   Mountains, East Antarctica. Memoirs of National Institute of Polar Research, Special Issue, 43,

761   116-132.

762   Kretz, R., 1983. Symbols for rock-forming minerals. American Mineralogist 68, 277-279.

763   Kullerud, K., 1996. Chlorine-rich amphiboles: interplay between amphibole composition and an

764   evolving fluid. European Journal of Mineralogy 8, 355-370.

765   Kusebauch, C., John, T., Barnes, J.D., Klügel, A., Austrheim, H.O., 2015. Halogen element and stable

766   chlorine isotope fractionation caused by fluid–rock interaction (Bamble Sector, SE Norway).

767   Journal of Petrology 56, 299-324.

768   Li, Z., Tainosho, Y., Shiraishi, K., Owada, M., 2003. Chemical characteristics of fluorine-bearing

769   biotite of early Paleozoic plutonic rocks from the Sør Rondane Mountains, East Antarctica.

770   Geochemical Journal 37, 145–161.

771   Li, Z., Du, Z., Yang, S., Chen, H., Song, B., Liu, D., 2006. First report of zircon SHRIMP U–Pb dating

772   from the Dufek granite in the Sør Rondane Mountains, East Antarctica. Journal of Zhejiang

773   University Science A (Suppl. II), 315–319.

774   Li, Z.L., Chen, H., Yang, S., Tainosho, Y., Shiraishi, K., Owada, M., 2007. Fluid components in

775   accessory minerals of Pan-African granitoids in the Sør Rondane Mountains, East Antarctica.

776   Journal of Zhejiang University Science A 8, 1004-1010.

777   Ludwig, K.R., 2012. User's manual for Isoplot 3.75. A geological toolkit for Microsoft Excel.

778   Berkeley Geochronology Center Special Publication No.5 (revision of January 30, 2012. 75

779   pp.).

780   Manning, C.E., Aranovich, L.Y., 2014. Brines at high pressure and temperature: Thermodynamic,

781   petrologic and geochemical effects. Precambrian Research 253, 6-16.

782   Markl, G., Bucher, K., 1998. Composition of fluids in the lower crust inferred from metamorphic salt

783   in lower crustal rocks. Nature 391, 781-783.

784   Mathez, E.A., Webster, J.D., 2005. Partitioning behavior of chlorine and fluorine in the system

785   apatite-melt-fluid. Geochimica et Cosmochimica Acta 69, 1275-1286.

786   Meert, J., 2003. A synopsis of events related to the assembly of eastern Gondwana. Tectonophysics

787   362, 1–40.

788   Mieth, M., Jacobs, J., Ruppel, A., Damaske, D., Läufer, A., Jokat, W., 2014. New detailed

789   aeromagnetic and geological data of eastern Dronning Maud Land: Implications for refining the

790   tectonic and structural framework of Sør Rondane, East Antarctica. Precambrian Research 245,

791   174-185.

792   Milord, I., Sawyer, E.W., Brown, M., 2001. Formation of diatexite migmatite and granite magma

793   during anatexis of semi-pelitic metasedimentary rocks: an example from St. Malo, France.

794   Journal of Petrology 42, 487-505.

795   Munoz, J.L., Swenson, A., 1981. Chrolide-hydroxyl exchange in biotite and estimation of relative

796   HCl/HF activities in hydrothermal fluids. Economic Geology 76, 2212-2221.

797   Munoz, J.L., 1992. Calculation of HF and HCl fugacities from biotite compositions: revised equations.

798   Geological Society of America, Abstract with Programs 24, A221.

799   Newton, R.C., Aranovich,L.Y., Hansen,E.C., Vandenheuvel,B.A., 1998. Hypersaline fluids in

800   Precambrian deep-crustal metamorphism. Precambrian Research 91, 41-63.

801   Newton, R.C., Touret, J.L.R., Aranovich, L.Y., 2014. Fluids and H_2O activity at the onset of granulite

802   facies metamorphism. Precambrian Research 253, 17-25.

803   Osanai, Y., Shiraishi, K., Takahashi, Y., Ishizuka, H., Tainosho, Y., Tsuchiya, N., Sakiyama, T.,

804   Kodama, S., 1992. Geochemical characteristics of metamorphic rocks from the central Sør

805   Rondane Mountains, East Antarctica. In: Yoshida, Y., Kaminuma, K., Shiraishi, K. (Eds.),

806   Recent Progress in Antarctic Earth Science. Terra Scientific Publishing Company, Tokyo, pp.

807   17–27.

808   Osanai, Y., Nogi, Y., Baba, S., Nakano, N., Adachi, T., Hokada, T., Toyoshima, T., Owada, M.,

809   Satish-Kumar, M., Kamei, A., Kitano, I., 2013. Geologic evolution of the Sør Rondane

810   Mountains, East Antarctica: Collision tectonics proposed based on metamorphic processes and

811   magnetic anomalies. Precambrian Research 234, 8-29.

812   Otsuji, N., Satish-Kumar, M., Kamei, A., Tsuchiya, N., Kawakami, T., Ishikawa, M., Grantham, G. H.,

813   2013. Late-Tonian to early-Cryogenian apparent depositional ages for metacarbonate rocks

814   from the Sør Rondane Mountains, East Antarctica. Precambrian Research 234, 257-278.

815   Otsuji, N., Satish-Kumar, M., Kamei, A., Takazawa, E., Tsuchiya, N., Grantham, G. H., Kawakami, T.,

816   Ishikawa, M., Osanai, Y., 2016. Sr and Nd Isotopic evidence in metacarbonate rocks for an

817   extinct Island arc - ocean system in East Antarctica. Journal of Mineralogical and Petrological

818   Sciences 111, 170-180.

819   Piccoli, P., Candela, P., 1994. Apatite in felsic rocks: a model for the estimation of initial halogen

820   concentrations in the Bishop Tuff (Long Valley) and Tuolumne intrusive suite (Sierra Nevada

821   Batholith) magmas. American Journal of Science 294, 92-135.

822   Rubatto, D., 2002. Zircon trace element geochemistry: partitioning with garnet and the link between

823   U–Pb ages and metamorphism. Chemical Geology 184, 123-138.

824   Rubenach, M.J., 2005. Relative timing of albitization and chlorine enrichment in biotite in Proterozoic

825   schists, Snake Creek anticline, Mount Isa inlier, Northeastern Australia. The Canadian

826   Mineralogist 43, 349-366.

827   Ruppel, A.S., Läufer, A., Jacobs, J., Elburg, M., Krohne, N., Damaske, D., Lisker, F., 2015. The Main

828   Shear Zone in Sør Rondane, East Antarctica: Implications for the late-Pan-African tectonic

829   evolution of Dronning Maud Land. Tectonics 34, 1290-1305.

830   Safonov, O.G., Kosova, S.A., Van Reenen, D.D., 2014. Interaction of biotite-amphibole gneiss with

831   H_2O-CO_2-(K, Na)Cl fluids at 550MPa and 750 and 800°C: Experimental study and applications

832   to dehydration and partial melting in the middle crust. Journal of Petrology 55, 2419-2456.

833   Selby, D., Nesbitt, B.E., 2000. Chemical composition of biotite from the Casino porphyry Cu-Au-Mo

834   mineralization, Yukon, Canada: evaluation of magmatic and hydrothermal fluid chemistry.

835   Chemical Geology 171, 77-93.

836   Shiraishi, K., Kojima, S., 1987. Basic and intermediate gneisses from the western part of the Sør

837   Rondane Mountains, East Antarctica. Proceedings of the NIPR symposium on Antarctic

838   Geosciences 1, 129-149.

839   Shiraishi, K., Asami, M., Ishizuka, H., Kojima, H., Kojima, S., Osanai, Y., Sakiyama, T., Takahashi,

840   Y., Yamazaki, M., Yoshikura, S., 1991. Geology and metamorphism of the Sør Rondane

841   Mountains, East Antarctica. In: Thomson, M.R.A., Crame, J.A., Thomson, J.W. (Eds.),

842   Geological Evolution of Antarctica. Cambridge University Press, Cambridge, pp. 77–82.

843   Shiraishi, K., Osanai, Y., Tainosho, Y., Takahashi, Y., Tsuchiya, N., Kojima, S., Yanai, K., Moriwaki,

844   K., 1992. Geological map of Widerøefjellet. Antarctic Geological Map Series, sheet 32, scale

845   1:100,000, National Institute of Polar Research, Tokyo.

846   Shiraishi, K., Osanai, Y., Ishizuka, H., Asami, M., 1997. Geological map of the Sør Rondane

847   Mountains, Antarctica. Antarctic Geological Map Series, sheet 35, scale 1:250,000, National

848   Institute of Polar Research, Tokyo.

849   Shiraishi, K., Dunkley, D.J., Hokada, T., Fanning, C.M., Kagami, H., Hamamoto, T., 2008.

850   Geochronological constrains on the Late Proterozoic to Cambrian crustal evolution of eastern

851   Dronning Maud Land, East Antarctica: a synthesis of SHRIMP U-Pb age and Nd model age

852   data. Geological Society of London, Special Publications 308, 21–67.

853   Spear, F.S., Kohn, M.J., Cheney, J.T., 1999. P-T paths from anatectic pelites. Contributions to

854   Mineralogy and Petrology 134, 17-32.

855   Tomkins, H.S., Powell, R., Ellis, D.J., 2007. The pressure dependence of the zirconium-in-rutile

856   thermometer. Journal of metamorphic Geology 25, 703-713.

857   Touret, J.L.R., Huizenga, J.M., 2011. Fluids in granulites. The Geological Society of America Memoir

858   207, 25-37.

859   Touret, J.L.R., Santosh, M., Huizenga, J.M., 2016. High-temperature granulites and supercontinents.

860   Geoscience Frontiers 7, 101-113.

861   Toyoshima, T., Osanai, Y., Baba, S., Hokada, T., Nakano, N., Adachi, T., Otsubo, M., Ishikawa, M.,

862   Nogi, Y., 2013. Sinistral transpressional and extensional tectonics in Dronning Maud Land,

863   East Antarctica, including the Sør Rondane Mountains. Precambrian Research 234, 30-46.

864   Tsuchiya, N., Ishikawa, M., Satish-Kumar, M., Kawakami, T., Kojima, H., Kaiden, H., Miura, H.,

865   Suganuma, Y., Abe, M., Sasaki, D., Chiba, M., Okada, Y., Hashizume, F., Grantham, G.,

866   Goderis, S., 2012. Report on geological fieldwork in the Sør Rondane Mountains, Eastern

867   Dronning Maud Land, 2009–2010 (JARE-51). Antarctic Record 56, 295–379.

868   Van den Berg, R., Huizenga, J.M., 2001. Fluids in granulites of the Southern Marginal Zone of the

869   Limpopo Belt, South Africa. Contributions to Mineralogy and Petrology 141, 529-545.

870   Watson, E.B., Brenan, J.M., 1987. Fluids in lithosphere, 1. Experimentally determined wetting

871   characteristics of CO_2-H_2O fluids and their implications for fluid transport, host-rock physical

872   properties and fluid inclusion formation. Earth and Planetary Science Letters 85, 594–615.

873   Webster, J.D., 1992. Fluid-melt interactions involving Cl-rich granites: Experimental study from 2 to 8

874   kbar. Geochimica et Cosmochimica Acta   56, 659-678.

875   Weinberg, R.F., Hasalová, P., 2015. Water-fluxed melting of the continental crust: A review. Lithos

876   212-215, 158-188.

877   Wu, C.-M., Zhang, J., Ren, L.-D., 2004. Empirical garnet-biotite-plagioclase-quartz (GBPQ)

878   geobarometry in medium- to high-grade metapelites. Journal of Petrology 45, 1907-1921.

879   Yardley, B.W.D., Barber, J.P., 1991. Melting reactions in the Connemara Schists: the role of water

880   infiltration in the formation of amphibolite facies migmatites. American Mineralogist 76, 848–

881   856.

882   Zack, T., Moraes, A.R., Kronz, A.A., 2004. Temperature dependence of Zr in rutile: empirical

883   calibration of a rutile thermometer. Contributions to Mineralogy and Petrology 148, 471-488.

884   Zhu, C., Sverjensky, D.A., 1991. Partitioning of F-Cl-OH between minerals and hydrothermal fluids.

885   Geochimica et Cosmochimica Acta 55, 1837-1858.

886   Zhu, C., Sverjensky, D.A., 1992. F-Cl-OH partitioning between biotite and apatite. Geochimica et

887   Cosmochimica Acta 56, 3435-3467.

888

889   **Figure captions**

890   Figure 1. (a) Gondwana amalgamation model by Neoproterozoic orogens. East African Orogen and

891   Kuunga Orogen (Meert, 2003) are shown. Position of the Sør Rondane Mountains is shown by

892   a star. (b) Geological map of the Sør Rondane Mountains, East Antarctica (modified after

893   Shiraishi et al., 1997, 2008; Osanai et al., 1992; 2013; Toyoshima et al., 2013; Ishikawa et al.,

894   2013), showing the location of Perlebandet. Chlorine concentrations of biotite (circles) and

895   amphibole (squares) in pelitic and mafic gneisses (Higashino et al., 2013a; 2015a) are also

896   shown. Warm color represents biotite or hornblende with higher-Cl contents. Note that Cl-rich

897   biotite and hornblende are localized near tectonic boundaries and shear zones. location 4;

898   location 4 of Higashino et al. (2013). The Main Tectonic Boundary (O) is after Osanai et al.

899   (2013) and the Main Tectonic Boundary (M) is after Mieth et al. (2014). (c) Geological map of

900   Perlebandet after Shiraishi et al. (1992). Sample localities are also shown.

901   Figure 2. (a) Garnet porphyroblast including abundant sillimanite needles in the core. Sillimanite is

902   also arranged along the gneissose structure of the matrix (top). Sample 2602D. Plane polarized

903   light (PPL). (b)-(o) Mode of occurrence of metamorphic minerals in a

904   garnet-sillimanite-biotite gneiss (sample 3001G). (b) Sillimanite including Zn-bearing spinel

905   overgrown by garnet. This microstructure is interpreted to represent staurolite breakdown.

906   Crossed polarized light (CPL). (c) Sillimanite porphyroblast with the inclusion-poor core and

907   inclusion-rich rim. Subgrain boundaries can be clearly observed. CPL. (d) Enlargement of the

908   dotted square in (c). Zn-bearing spinel is included in the inclusion-rich rim of the sillimanite

909   porphyroblast. Cl-rich biotite and ilmenite are included in the inclusion-poor core of the

910   sillimanite. PPL. (e) Sillimanite, andalusite and biotite replacing garnet. PPL. (f) Garnet rim

911   replaced by biotite + andalusite intergrowth with minor fibrolitic sillimanite. PPL. (g) BSE

912   image of breakdown microstructure of garnet replaced by biotite, plagioclase, andalusite +

913   quartz intergrowth, kyanite and muscovite. Outlines of kyanite grains are indicated by red lines.

914   (h) Panchromatic CL image of the same area as (g). Warm colors indicate higher CL intensity.

915   Note the high CL intensity of kyanite compared to low CL intensity of andalusite. (i) BSE

916   image of breakdown microstructure of garnet replaced by biotite, plagioclase, quartz,

917   andalusite, kyanite and sillimanite. Sillimanite includes Zn-bearing spinel grains. Outline of

918   kyanite grains are indicated by red lines. (j) Panchromatic CL image of the same area as (i).

919   Warm colors indicate higher CL intensity. Note the high CL intensity of kyanite compared to

920   moderate and low intensity of sillimanite and andalusite, respectively. (k) Garnet including

921   sillimanite and Zn-bearing spinel, which is partly replaced by the aggregate of Bt + And + Sil +

922   Crn + Spl + Ms at the rim. PPL. (l) CPL of (k). Sillimanite is separately included in garnet,

923   whereas andalusite and sillimanite are found in the replacement microstructure of garnet. (m)

924   Garnet that is including Zn-bearing spinel is partly replaced by the retrograde aggregate of Bt +

925   And + Ky + Sil + Spl. PPL. (n) CPL of (m). Note that andalusite and kyanite (right), as well as

926   andalusite and sillimanite (center) are in direct contact. (o) A BSE image of rutile partly

927   replaced by ilmenite. Both of them are included in garnet.

928   Figure 3. Plots showing the variations of biotite composition depending on the mode of occurrence. (a)

929   TiO_2 (wt.%) vs X_{Mg} plot for sample 3001G. (b) Cl (wt.%) vs X_{Mg} plot for sample 3001G. (c)

930   TiO_2 (wt.%) vs X_{Mg} plot for sample 3001B. (d) Cl (wt.%) vs X_{Mg} plot for sample 3001B. (e)

931   TiO_2 (wt.%) vs X_{Mg} plot for sample 2601C. (b) Cl (wt.%) vs X_{Mg} plot for sample 2601C.

932   Figure 4. X-ray elemental mappings and BSE images showing the mode of occurrence of Cl-rich

933   biotite from samples 3001B (a-c) and 2601C (d-f). (a) BSI of garnet including Cl-rich biotite

934   and apatite. Garnet is partly replaced by retrograde biotite at the rim and along the cracks. (b)

935   X-ray elemental map of Cl for the area including (a). Cl-rich biotite (yellow to yellowish green)

936   is present as inclusions in garnet and as a matrix phase (especially at the top of the map).

937   Retrograde biotite replacing garnet has lower Cl content (light blue). Apatite included in garnet

938   is enriched in Cl. (c) X-ray elemental map of Mg for the same area as (b). Some of the Cl-rich

939   biotite grains included in garnet show higher Mg content (red) than the matrix biotite (greenish

940   yellow). (d) BSI of garnet partly replaced by biotite-plagioclase intergrowths. (e) X-ray

941   elemental maps of Cl for the area including (d). Cl-rich biotite is present as an isolate matrix

942   phase (yellowish green). Moderately Cl-bearing biotite is present as a biotite-plagioclase

943   intergrowth replacing garnet (light blue). (f) X-ray elemental map of Mg for the same area as

944   (d).

945   Figure 5. CL images of zircon from Perlebandet. (a)-(h) Sample 3001G. (i)-(l) Sample 3001B. (m)-(t)

946   Sample 2601C. Red circles represent the pits of the LA-ICPMS U-Pb dating (5 μm) and

947   numbers given are the ^{206}Pb/^{238}U age ± 2S.D. error [better than 95-105% concordance, where

948   concordance = (^{206}Pb/^{238}U age)*100/(^{207}Pb/^{235}U age)] and Th/U ratio. *in Grt bd*; zircon present

949   in garnet breakdown microstructure developed around garnet. *matrix*; zircon present in the

950   matrix. *in Grt/Sil rim*; zircon included in garnet/sillimanite rim. *** Ma; discordant data point.

951   Figure 6. (a)-(c) Concordia diagrams and probability density plot (inset) for the LA-ICPMS U-Pb

952   zircon dating. Concordant data (concordance = 95-105%) are used to construct the probability

953   density plot. Color variation of the error ellipses represents Th/U ratio of the dated spots. Note

954   that ages older than ca. 1200 Ma is absent in all samples. (a) Sample 3001G. (b) Sample 3001B.

955   (c) Sample 2601C. (d) A plot showing the relationship between concordant age vs Th/U ratio of

956   the analyzed spots.

957   Figure 7. Pressure-temperature diagram showing a *P-T-t* path (red arrows) for Perlebandet rocks.

958   Evolution of microstructure for sample 3001G is given as sketches (1)-(3) and change of fluid

959   compositions along the *P-T-t* path is also indicated. Note that Cl-rich fluid is present from

960   prograde metamorphism. Petrogenetic grid for the NaKFMASH system with contours of

961   Mg/(Fe+Mg) = 0.1-0.4 in garnet in divariant Als + Grt + Bt assemblage are from Spear et al.

962   (1999). Prograde, peak and retrograde *P-T* estimates by the Grt-Bt geothermometer (GB)

963   (Holdaway et al., 1997; Holdaway, 2000) and the GASP geobarometer (Holdaway, 2001) are

964   shown as gray, red and black squares, respectively. Peak *P-T* estimate by the Zr-in-rutile

965   geothermometer (Tomkins et al., 2007), the Grt-Bt geothermometer (Holdaway et al., 1997;

966   Holdaway, 2000) and the GASP geobarometer (Holdaway, 2001) is shown by a red broken

967   diamond. Zr-in-rutile$_{1550}$ represents a result of the Zr-in-rutile geothermometer (Tomkins et al.,

968   2007) for 1550 ppm Zr, and Zr-in-rutile$_{2200}$ represents that for 2200 ppm Zr. Retrograde *P-T*

969   estimates by the Grt-Bt geothermometer (Holdaway et al., 1997; Holdaway, 2000) and the

970   GBPQ geobarometer (Wu et al., 2004) using compositions of garnet rims and biotite and

971   plagioclase in the biotite-plagioclase intergrowths are shown as solid squares, where green,

972   blue and brown squares are from samples 3001B, 3001G and 2601C, respectively. These

54

973   estimates would accompany errors of ±50 ℃ and ±0.1 GPa, which are not shown for

974   simplicity. Numbers of the reactions correspond to those in the text. Reactions (4)-(6) are not

975   shown.

976   Figure 8. Simplified cross section showing the tectonic model for the continental collision in the SRM,

977   modified after Osanai et al. (2013). Chlorine-rich fluid infiltration in Perlebandet presumably

978   took place at the uppermost part of the footwall of the MBT. Chlorine-rich fluid infiltration in

979   Balchenfjella is dated to be at ca. 603 Ma (Higashino et al., 2013), and would be an older event

980   than that in Perlebandet (ca. 580 Ma). BDF: Balchen Detachment Fault (Ishikawa et al., 2013).

981   [1] This study, [2] Higashino et al. (2015a), [3] Higashino et al. (2013).

982   Table 1. Representative mineral analysis of biotite, garnet and plagioclase from samples 3001G,

983   3001B and 2601C. The $\log[f(H_2O)/f(HCl)]$ and $\log[f(H_2O)/f(HF)]$ values of the fluid that

984   possibly coexisted with Cl-bearing biotite (Munoz, 1992) are also shown. [1] Based on Munoz

985   (1992). [2] Temperature used in calculating $\log[f(H_2O)/f(HCl)]$ and $\log[f(H_2O)/f(HF)]$ values of

986   the fluid possibly coexisted with biotite. Temperature was estimated using the Grt-Bt

987   geothermometer (Holdaway et al., 1997; Holdaway, 2000) and the GASP (Holdaway, 2001)

988   and Grt-Bt-Pl-Qtz (Wu et al., 2004) geobarometers. [3] Temperature was estimated using

989   Zr-in-rutile geothermometer by Tomkins et al. (2006) and GASP geobarometer (Holdaway,

990   2001).

991   Supplementary Table 2. Summary of the results of LA-ICPMS U-Pb zircon dating.
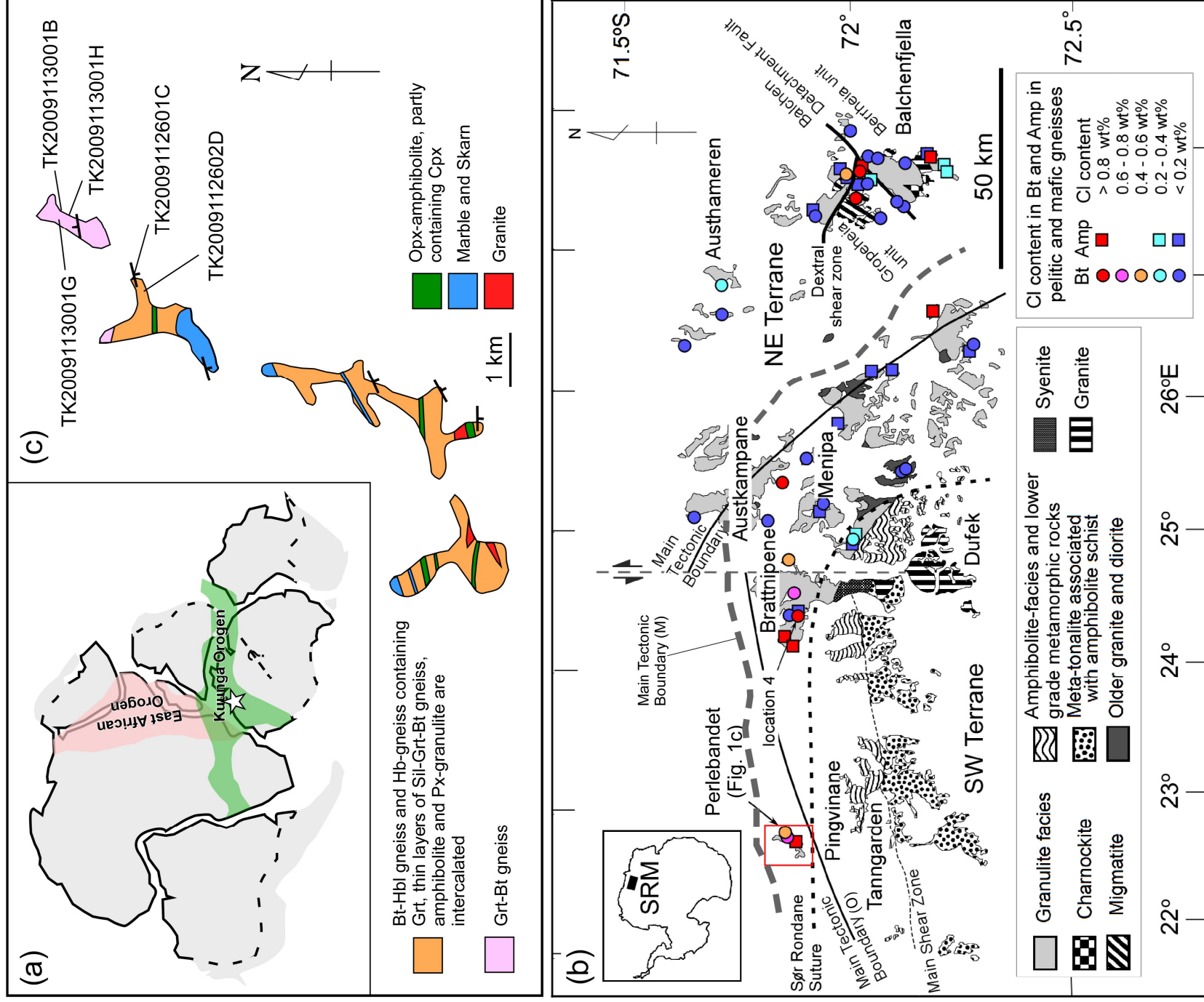
Kawakami et al. Fig. 1
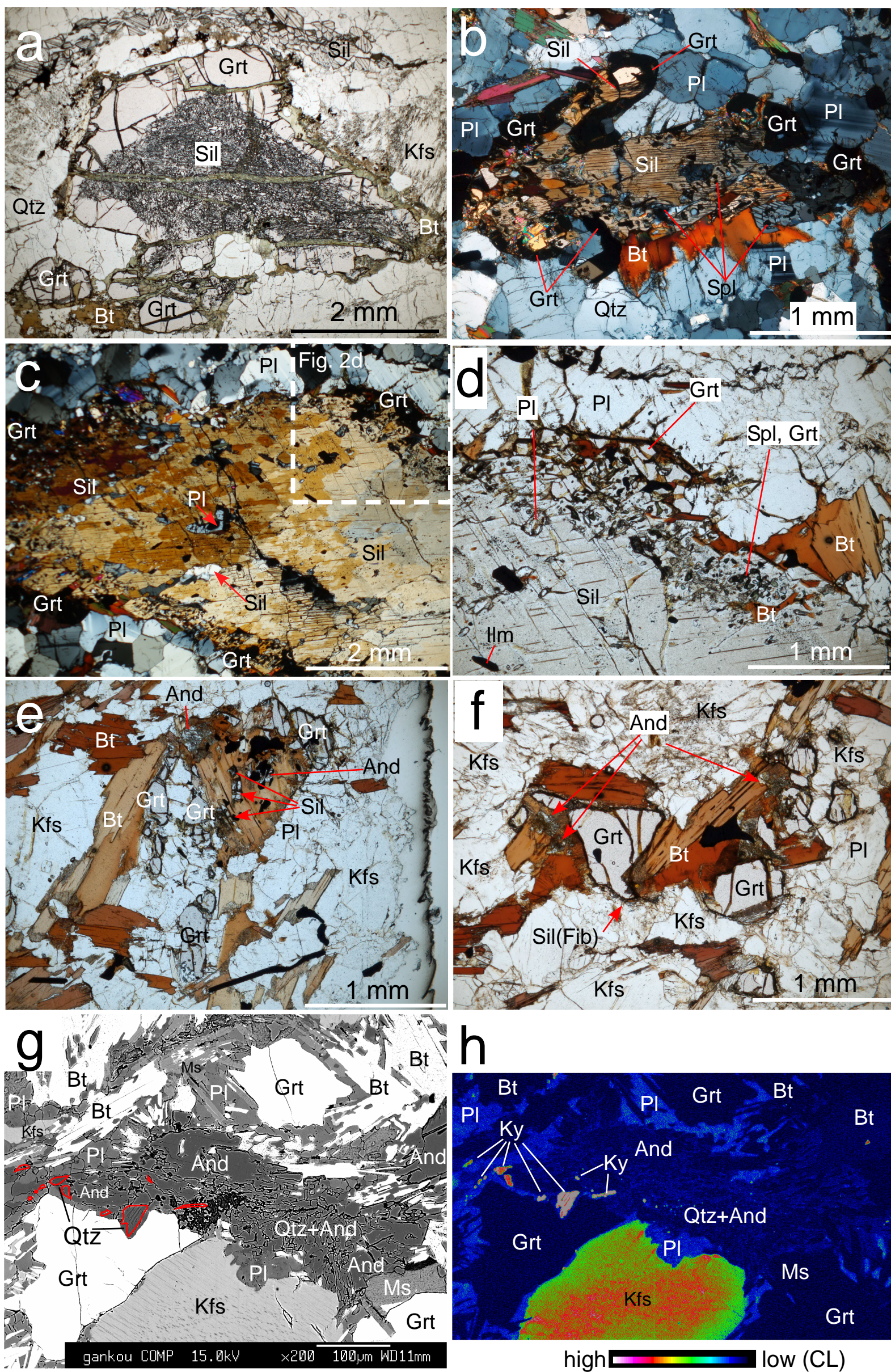
Kawakami et al. Fig. 2
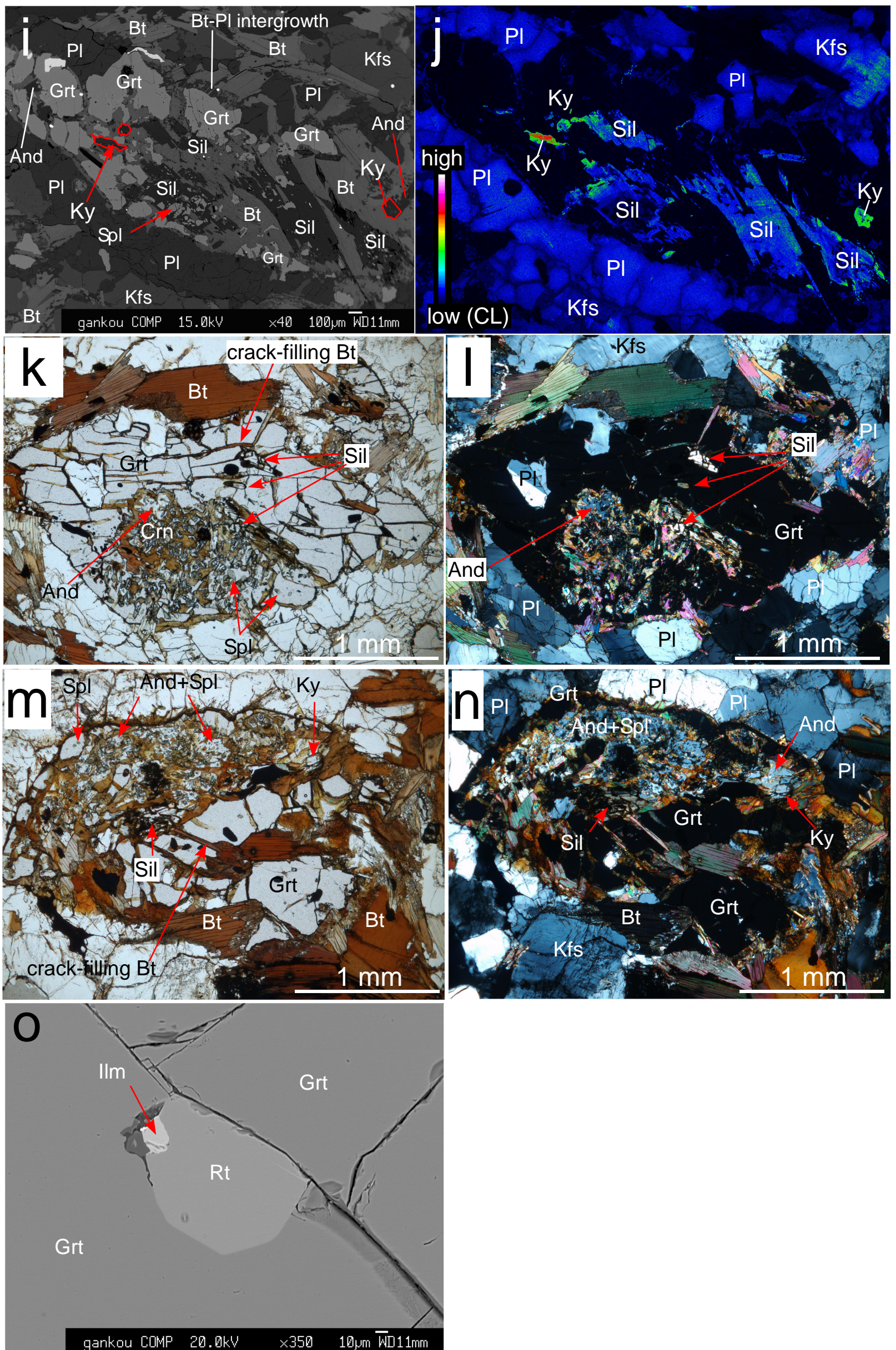
Kawakami et al Fig 2 (continued)
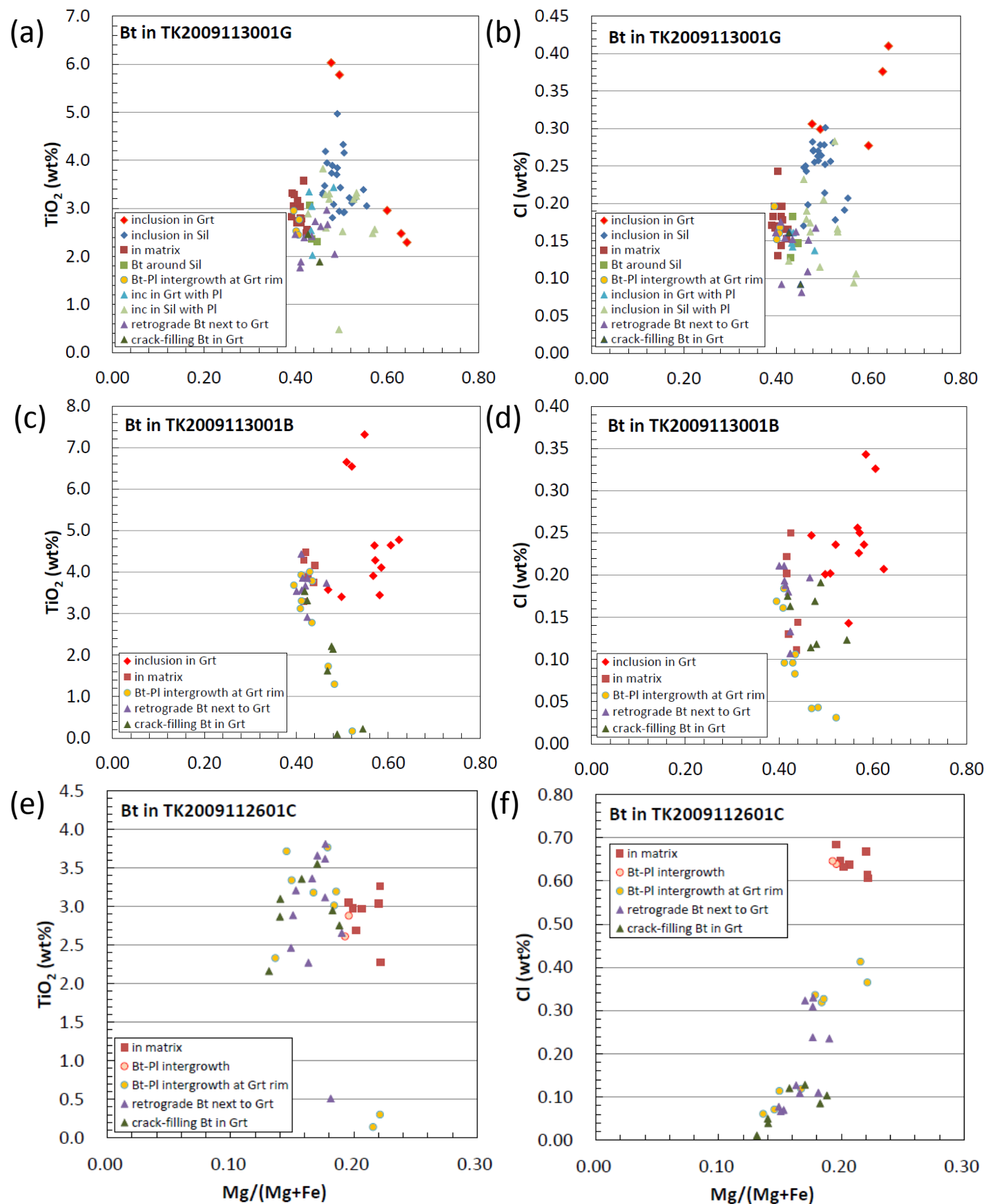
Kawakami et al. Fig 7

Kawakami et al. Fig. 3
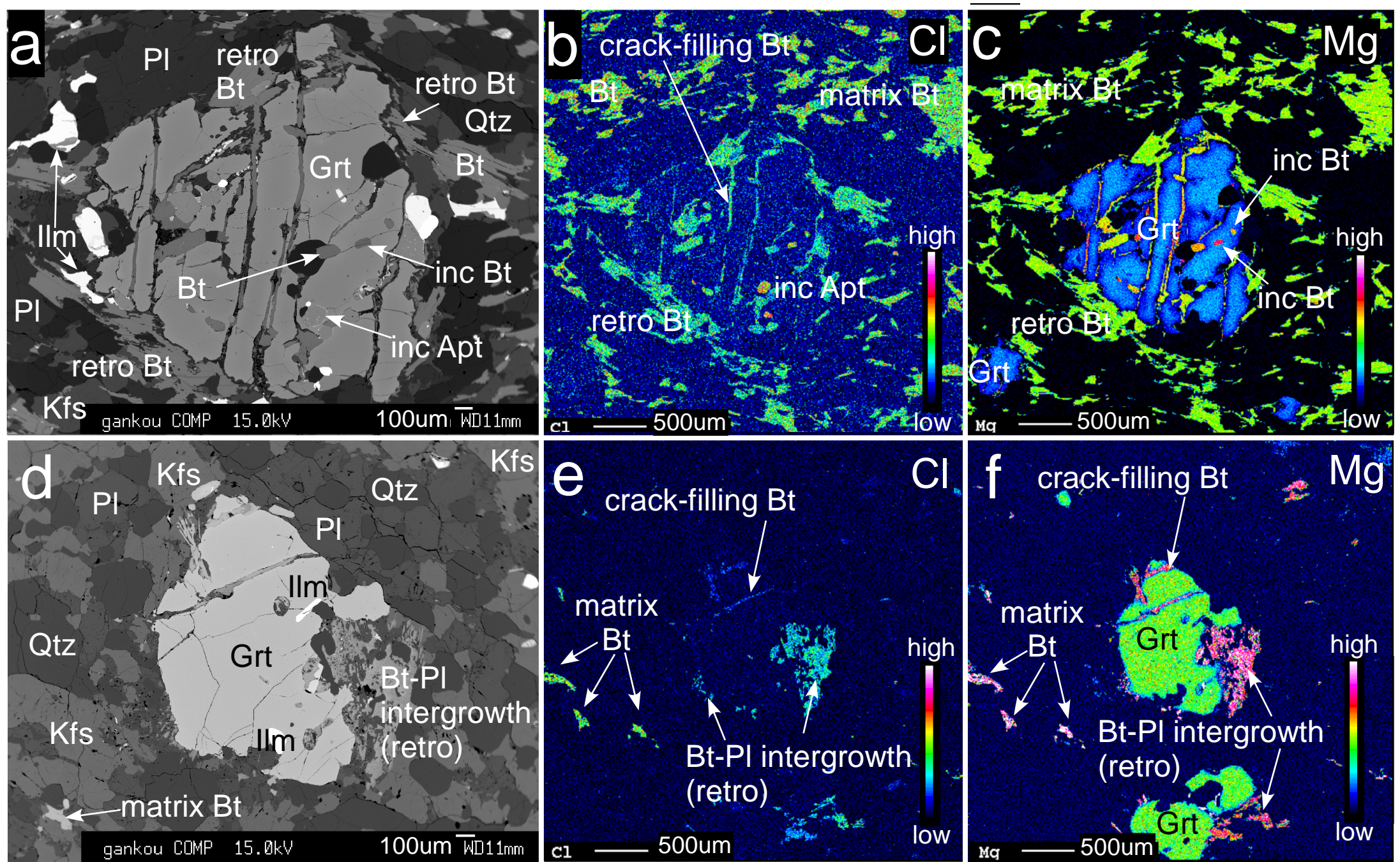
Kawakami et al Fig 4
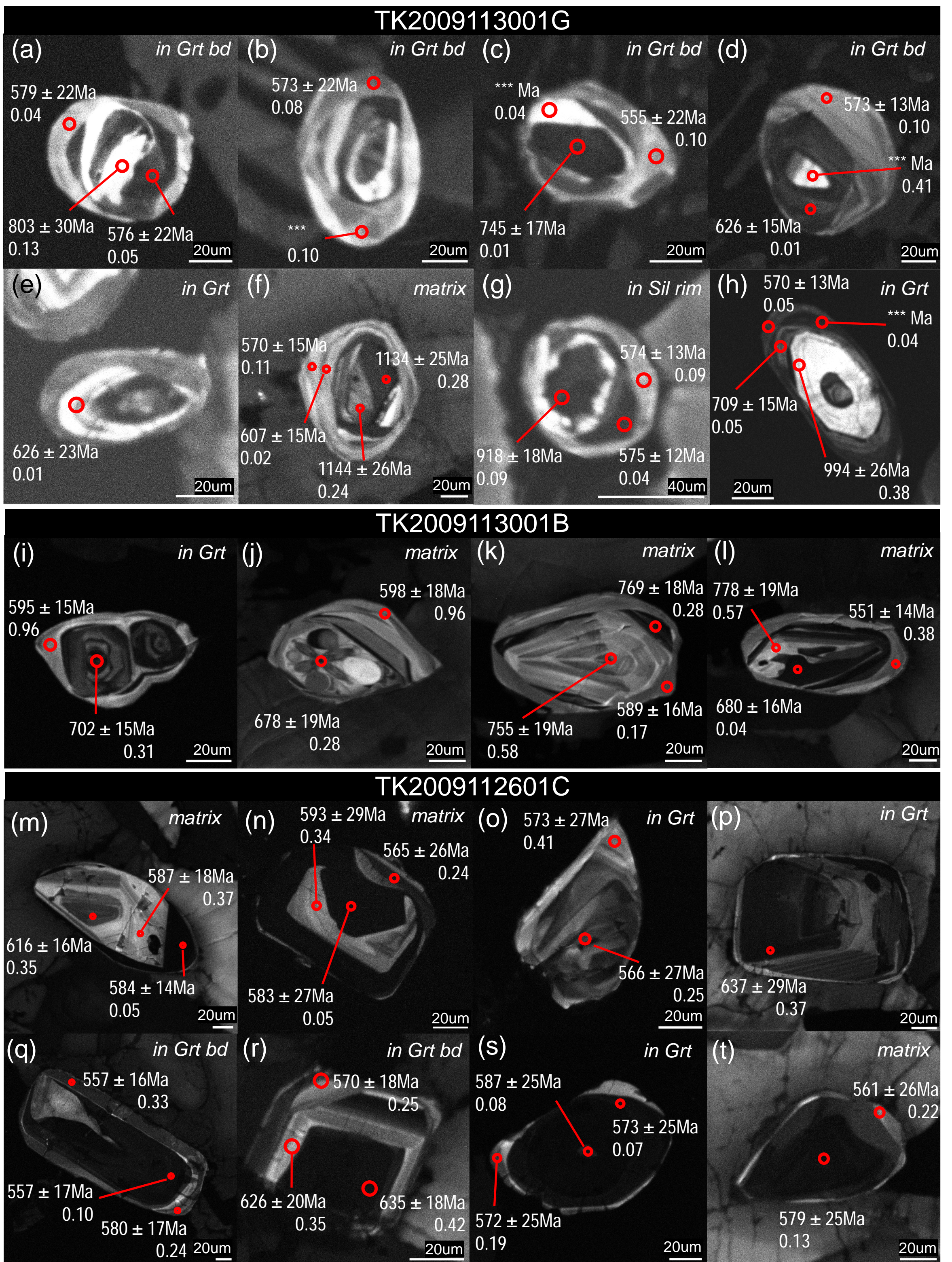
Fig. 5 Kawakami et al.

Kawakami et al. Fig. 6

Kawakami et al. Fig 7

Fig. 8 Kawakami et al.

Table (part 1)

	Pl	Pl	Pl	Pl	Grt	Grt	Grt	Grt	Spl	Bt	Bt	Bt	Bt	Bt	Bt	Bt	Grt	Grt	Pl	Pl	Pl
sample	TK2009113001G																TK2009112601C				
mineral	Pl	Pl	Pl	Pl	Grt	Grt	Grt	Grt	Spl	Bt	Bt	Bt	Bt	Bt	Bt	Bt	Grt	Grt	Pl	Pl	Pl
occurrence	inclusion in Sil	inclusion in Sil	Pl moat around Sil (Sil side)	Pl moat around Sil (Kfs side)	overgrowth on Sil	overgrowth on Sil	in matrix	in matrix	inclusion in Sil rim	inclusion in Grt	inclusion in Sil	in matrix (isolated)	in matrix (isolated)	Bt-Pl intergrowth replacing Grt	retrograde Bt next to Grt	crack-filling Bt in Grt	in matrix	in matrix	in matrix	in matrix	Bt-Pl intergrowth replacing Grt
core/rim	core	rim			core	rim	core	rim									rim	core	rim	core	
SiO₂	59.65	59.71	61.01	62.14	38.95	37.76	37.81	37.48	0.14	37.70	34.78	36.68	35.85	35.29	34.92	35.44	38.00	38.33	61.41	61.19	61.89
TiO₂	0.00	0.06	0.00	0.10	0.00	0.02	0.05	0.00	0.00	2.29	4.19	3.15	3.58	2.76	2.39	1.89	0.01	0.08	0.01	0.00	0.03
Al₂O₃	26.02	25.63	24.76	23.72	22.00	21.18	21.72	21.26	61.03	19.12	18.50	18.91	19.30	19.04	18.94	20.28	21.23	21.10	23.93	24.06	23.88
Cr₂O₃	0.00	0.00	0.00	0.00	0.02	0.08	0.00	0.06	0.11	0.00	0.06	0.10	0.05	0.07	0.09	0.01	0.00	0.04	0.00	0.00	0.00
FeO	0.11	0.05	0.00	0.02	32.31	36.58	35.68	36.04	27.07	13.57	19.09	20.20	20.43	20.39	21.17	18.59	33.74	31.81	0.06	0.02	0.38
ZnO	n.d.	n.d.	n.d.	n.d.	n.d.	n.d.	n.d.	n.d.	6.03	n.d.	n.d.	n.d.	n.d.	n.d.	n.d.	n.d.	n.d.	n.d.	n.d.	n.d.	n.d.
MnO	0.01	0.00	0.02	0.00	0.62	1.44	0.84	1.83	0.06	0.11	0.04	0.02	0.06	0.04	0.14	0.05	0.77	0.82	0.03	0.00	0.02
MgO	0.00	0.00	0.00	0.00	4.90	2.38	3.26	2.48	5.56	13.74	9.33	7.68	8.21	7.89	7.90	8.64	1.48	1.95	0.01	0.00	0.02
CaO	7.78	6.92	6.54	5.52	2.29	1.49	2.27	1.44	0.08	0.02	0.00	0.00	0.01	0.00	0.00	0.00	6.36	7.17	5.90	5.94	5.60
BaO	0.15	0.06	0.09	0.02	0.11	0.06	0.11	0.00	0.00	0.06	0.30	0.08	0.16	0.05	0.00	0.00	0.09	0.00	0.02	0.00	0.00
Na₂O	7.24	7.65	7.95	8.69	0.00	0.02	0.04	0.02	0.00	0.19	0.05	0.12	0.10	0.11	0.12	0.16	0.07	0.00	8.14	8.20	8.35
K₂O	0.23	0.19	0.25	0.16	0.02	0.01	0.00	0.00	0.04	9.13	9.58	9.63	9.56	10.01	9.77	9.87	0.01	0.03	0.28	0.15	0.15
F	n.d.	n.d.	n.d.	n.d.	n.d.	n.d.	n.d.	n.d.	n.d.	0.36	0.08	0.06	0.09	0.16	0.07	0.16	n.d.	n.d.	n.d.	n.d.	n.d.
Cl	n.d.	n.d.	n.d.	n.d.	n.d.	n.d.	n.d.	n.d.	n.d.	0.41	0.24	0.24	0.17	0.17	0.15	0.09	n.d.	n.d.	n.d.	n.d.	n.d.
-O≡F	n.d.	n.d.	n.d.	n.d.	n.d.	n.d.	n.d.	n.d.	n.d.	0.15	0.03	0.03	0.04	0.07	0.03	0.07	n.d.	n.d.	n.d.	n.d.	n.d.
-O≡Cl	n.d.	n.d.	n.d.	n.d.	n.d.	n.d.	n.d.	n.d.	n.d.	0.09	0.05	0.05	0.04	0.04	0.03	0.02	n.d.	n.d.	n.d.	n.d.	n.d.
Total	101.18	100.26	100.62	100.37	101.22	101.03	101.78	100.61	100.04	96.51	96.16	96.80	97.48	95.87	95.60	95.09	101.76	101.32	99.78	99.56	100.31
number of O	8	8	8	8	12	12	12	12	4	22	22	22	22	22	22	22	12	12	8	8	8
Si	2.64	2.66	2.70	2.75	3.03	3.02	2.98	3.01	0.00	5.50	5.28	5.52	5.37	5.40	5.37	5.40	3.01	3.03	2.73	2.73	2.74
Ti	0.00	0.00	0.00	0.00	0.00	0.00	0.00	0.00	0.00	0.25	0.48	0.36	0.40	0.32	0.28	0.22	0.00	0.00	0.00	0.00	0.00
Al	1.36	1.34	1.29	1.24	2.02	2.00	2.02	2.01	2.00	3.29	3.31	3.35	3.41	3.43	3.43	3.64	1.98	1.96	1.26	1.27	1.25
Cr	0.00	0.00	0.00	0.00	0.00	0.00	0.00	0.00	0.00	0.00	0.01	0.01	0.01	0.01	0.01	0.00	0.00	0.00	0.00	0.00	0.00
Fe	0.00	0.00	0.00	0.00	2.10	2.45	2.36	2.42	0.63	1.66	2.42	2.54	2.56	2.61	2.72	2.37	2.23	2.10	0.00	0.00	0.01
Mn	0.00	0.00	0.00	0.00	0.04	0.10	0.06	0.12	0.00	0.01	0.00	0.00	0.00	0.00	0.02	0.01	0.05	0.05	0.00	0.00	0.00
Mg	0.00	0.00	0.00	0.00	0.57	0.28	0.38	0.30	0.23	2.99	2.11	1.72	1.83	1.80	1.81	1.96	0.17	0.23	0.00	0.00	0.00
Ca	0.37	0.33	0.31	0.26	0.19	0.13	0.19	0.12	0.01	0.00	0.00	0.00	0.00	0.00	0.00	0.00	0.54	0.61	0.28	0.28	0.27
Ba	0.00	0.00	0.00	0.00	0.00	0.00	0.00	0.00	0.00	0.00	0.02	0.00	0.01	0.00	0.00	0.00	0.00	0.00	0.00	0.00	0.00
Zn	n.d.	n.d.	n.d.	n.d.	n.d.	n.d.	n.d.	n.d.	0.12	n.d.	n.d.	n.d.	n.d.	n.d.	n.d.	n.d.	n.d.	n.d.	n.d.	n.d.	n.d.
Na	0.62	0.66	0.68	0.74	0.00	0.00	0.01	0.00	0.00	0.05	0.02	0.03	0.03	0.03	0.04	0.05	0.01	0.00	0.70	0.71	0.72
K	0.01	0.01	0.01	0.01	0.00	0.00	0.00	0.00	0.00	1.70	1.85	1.85	1.83	1.95	1.92	1.92	0.00	0.00	0.02	0.01	0.01
F	n.d.	n.d.	n.d.	n.d.	n.d.	n.d.	n.d.	n.d.	n.d.	0.17	0.04	0.03	0.04	0.08	0.04	0.08	n.d.	n.d.	n.d.	n.d.	n.d.
Cl	n.d.	n.d.	n.d.	n.d.	n.d.	n.d.	n.d.	n.d.	n.d.	0.10	0.06	0.06	0.04	0.04	0.04	0.02	n.d.	n.d.	n.d.	n.d.	n.d.
Total cation	5.00	5.00	5.00	5.01	7.96	7.98	8.01	7.99	2.99	15.48	15.51	15.39	15.45	15.56	15.60	15.55	8.01	7.99	5.00	5.00	5.00
Mg/(Fe$_{total}$+Mg)					0.21	0.10	0.14	0.11	0.27	0.64	0.47	0.40	0.42	0.41	0.40	0.45	0.07	0.10			
An	37.0	33.0	31.0	25.7															28.2	28.3	26.8
$\log(f_{H2O}/f_{HCl})$ of fluid [*1]										3.65	3.94			4.24	4.28						
$\log(f_{H2O}/f_{HCl})$ of fluid [*2]										0.12	1.19			2.19	2.25						
$\log(f_{H2O}/f_{HF})$ of fluid [*1]										4.31	5.07			5.12	5.46						
Temperature (°C)										800[*4]	700[*3]			580[*3]	580[*3]						

Table (part 2)

	Bt	Bt	Bt	Bt	Bt	Bt	Grt	Grt	Pl	Pl	Bt	Bt	Bt	Bt	Bt	Bt	Bt	Bt
sample	TK2009112601C						TK2009113001B											
mineral	Bt	Bt	Bt	Bt	Bt	Bt	Grt	Grt	Pl	Pl	Bt	Bt	Bt	Bt	Bt	Bt	Bt	Bt
occurrence	in matrix	in matrix	Bt-Pl intergrowth replacing Grt	Bt-Pl intergrowth replacing Grt	retrograde Bt next to Grt	crack-filling Bt in Grt	in matrix	in matrix	in matrix	Bt-Pl intergrowth replacing Grt	inclusion in Grt	inclusion in Grt	in matrix	in matrix	in matrix (near Grt)	Bt-Pl intergrowth replacing Grt	retrograde Bt next to Grt	crack-filling Bt in Grt
core/rim							core	rim	core						rim			
SiO₂	35.22	34.90	34.57	34.90	34.77	33.93	38.63	37.82	59.05	54.60	37.27	38.17	37.25	37.06	36.33	37.24	35.79	36.52
TiO₂	2.28	3.12	3.72	0.04	0.51	2.95	0.06	0.11	0.04	0.07	4.11	3.91	4.16	3.75	4.29	0.17	3.56	0.09
Al₂O₃	17.88	16.62	16.87	18.70	19.64	17.22	22.05	21.69	25.41	28.26	16.65	15.82	16.24	16.59	16.91	18.54	17.58	19.49
Cr₂O₃	0.04	0.01	0.03	0.04	0.00	0.00	0.00	0.00	0.00	0.04	0.00	0.04	0.01	0.03	0.02	0.05	0.00	0.02
FeO	27.96	31.02	31.10	28.37	27.47	29.95	32.35	33.11	0.05	0.33	15.95	17.35	20.95	21.62	22.84	19.80	22.46	21.06
ZnO	n.d.	n.d.	n.d.	n.d.	n.d.	n.d.	n.d.	n.d.	n.d.	n.d.	n.d.	n.d.	n.d.	n.d.	n.d.	n.d.	n.d.	n.d.
MnO	0.16	0.00	0.00	0.02	0.00	0.08	0.74	0.92	0.04	0.02	0.00	0.00	0.00	0.00	0.00	0.00	0.00	0.18
MgO	4.47	3.74	2.97	4.52	3.41	3.76	4.70	2.99	0.01	0.00	12.61	12.77	9.24	9.44	9.14	12.12	8.82	11.30
CaO	0.00	0.03	0.01	0.11	0.02	0.04	3.45	4.48	7.48	11.12	0.05	0.01	0.00	0.01	0.00	0.04	0.00	0.05
BaO	0.13	0.06	0.12	0.00	0.00	0.17	0.00	0.01	0.00	0.09	0.34	0.13	0.14	0.13	0.17	0.00	0.00	0.00
Na₂O	0.05	0.04	0.03	0.08	0.04	0.09	0.00	0.02	7.34	5.24	0.08	0.07	0.10	0.08	0.04	0.05	0.02	0.06
K₂O	8.19	7.49	7.92	7.51	9.53	7.20	0.00	0.00	0.19	0.14	8.07	8.12	8.27	8.12	7.88	8.18	8.16	8.23
F	0.06	0.00	0.00	0.18	0.00	0.00	n.d.	n.d.	n.d.	n.d.	0.20	0.30	0.08	0.04	0.00	0.12	0.00	0.10
Cl	0.61	0.24	0.07	0.37	0.11	0.09	n.d.	n.d.	n.d.	n.d.	0.34	0.26	0.14	0.11	0.22	0.03	0.19	0.19
-O≡F	0.03	0.00	0.00	0.08	0.00	0.00	n.d.	n.d.	n.d.	n.d.	0.09	0.13	0.03	0.02	0.00	0.05	0.00	0.04
-O≡Cl	0.14	0.05	0.02	0.08	0.02	0.02	n.d.	n.d.	n.d.	n.d.	0.08	0.06	0.03	0.03	0.05	0.01	0.04	0.04
Total	96.87	97.22	97.45	94.94	95.47	95.46	101.98	101.14	99.62	99.91	95.52	96.79	96.50	96.93	97.77	96.28	96.54	97.20
number of O	22	22	22	22	22	22	12	12	8	8	22	22	22	22	22	22	22	22
Si	5.49	5.47	5.42	5.53	5.49	5.40	3.00	2.99	2.65	2.47	5.55	5.63	5.61	5.56	5.44	5.55	5.42	5.44
Ti	0.27	0.37	0.44	0.04	0.06	0.35	0.00	0.01	0.00	0.00	0.46	0.43	0.47	0.42	0.48	0.02	0.41	0.01
Al	3.29	3.07	3.12	3.49	3.66	3.23	2.02	2.02	1.34	1.51	2.92	2.75	2.88	2.93	2.99	3.26	3.14	3.42
Cr	0.01	0.00	0.00	0.01	0.00	0.00	0.00	0.00	0.00	0.00	0.00	0.01	0.00	0.00	0.00	0.01	0.00	0.00
Fe	3.65	4.07	4.08	3.76	3.63	3.99	2.10	2.19	0.00	0.01	1.99	2.14	2.64	2.71	2.86	2.47	2.85	2.62
Mn	0.02	0.00	0.01	0.00	0.00	0.01	0.05	0.06	0.00	0.00	0.00	0.00	0.00	0.00	0.00	0.00	0.00	0.02
Mg	1.04	0.87	0.69	1.07	0.80	0.89	0.54	0.35	0.00	0.00	2.80	2.81	2.07	2.11	2.04	2.69	1.99	2.51
Ca	0.00	0.00	0.00	0.02	0.00	0.01	0.29	0.38	0.36	0.54	0.01	0.00	0.00	0.00	0.00	0.01	0.00	0.01
Ba	0.01	0.00	0.01	0.00	0.00	0.01	0.00	0.00	0.00	0.00	0.02	0.01	0.01	0.01	0.01	0.00	0.00	0.00
Zn	n.d.	n.d.	n.d.	n.d.	n.d.	n.d.	n.d.	n.d.	n.d.	n.d.	n.d.	n.d.	n.d.	n.d.	n.d.	n.d.	n.d.	n.d.
Na	0.01	0.01	0.01	0.02	0.01	0.03	0.00	0.00	0.64	0.46	0.02	0.03	0.03	0.02	0.01	0.01	0.01	0.02
K	1.63	1.50	1.59	1.52	1.92	1.46	0.00	0.00	0.01	0.01	1.53	1.53	1.59	1.55	1.51	1.56	1.58	1.56
F	0.03	0.00	0.00	0.09	0.00	0.00	n.d.	n.d.	n.d.	n.d.	0.10	0.14	0.04	0.02	0.00	0.06	0.00	0.05
Cl	0.16	0.06	0.02	0.10	0.03	0.02	n.d.	n.d.	n.d.	n.d.	0.09	0.06	0.04	0.03	0.06	0.01	0.05	0.05
Total cation	15.41	15.38	15.37	15.46	15.58	15.38	7.99	8.00	5.00	5.01	15.31	15.34	15.29	15.33	15.34	15.58	15.39	15.63
Mg/(Fe$_{total}$+Mg)	0.22	0.18	0.15	0.22	0.18	0.18	0.21	0.14			0.59	0.57	0.44	0.44	0.42	0.52	0.41	0.49
An									35.6	53.6								
$\log(f_{H2O}/f_{HCl})$ of fluid [*1]			4.19	3.50	4.02						3.70	3.82				4.95	4.09	
$\log(f_{H2O}/f_{HCl})$ of fluid [*2]			2.02	1.14	1.76						0.31	0.47				2.32	1.74	
$\log(f_{H2O}/f_{HF})$ of fluid [*1]			–	4.26	–						4.52	4.33				5.17	–	
Temperature (°C)			760[*3]	760[*3]	760[*3]						800[*4]	800[*4]				640[*3]	640[*3]	

	occurrence	zoning	$^{207}Pb/^{235}U$	error (± 2S.D.)	$^{206}Pb/^{238}U$	error (± 2S.D.)	Error correlation	$^{207}Pb/^{206}Pb$	error (± 2S.D.)	$^{207}Pb/^{235}U$ age (Ma)	error (± 2S.D., Ma)	$^{206}Pb/^{238}U$ age (Ma)	error (± 2S.D., Ma)	$^{207}Pb/^{206}Pb$ age (Ma)	error (± 2S.D., Ma)	Concncordance (%)	Th/U	U (ppm)	error (± 2S.D., ppm)	Th (ppm)	error (± 2S.D., ppm)	Pb (ppm)	error (± 2S.D., ppm)
TK2009112601-51A	inc in garnet	core	0.788945	0.039112	0.095355	0.004257	0.901	0.060007	0.001293	591	22	587	25	604	47	101	0.08	3121	448	234	67	375	304
TK2009112601-51B		rim	0.762783	0.05415	0.092749	0.004298	0.653	0.059647	0.003208	576	32	572	25	591	121	101	0.19	322	46	60	17	39	32
TK2009112601-51C		mantle	0.782543	0.040865	0.092992	0.004169	0.859	0.061032	0.001634	587	24	573	25	640	59	102	0.07	1624	233	121	35	190	155
TK2009112601-53A	in matrix	core	0.755302	0.038372	0.093941	0.004201	0.880	0.058313	0.001405	571	22	579	25	542	54	99	0.13	2270	326	292	84	272	221
TK2009112601-53B		rim	0.751175	0.048011	0.090952	0.004444	0.764	0.0599	0.002468	569	28	561	26	600	92	101	0.22	633	69	142	31	76	57
TK2009112601-55A		core	0.87678	0.050424	0.102448	0.004635	0.787	0.06207	0.002204	639	28	629	27	677	78	102	0.37	710	102	261	75	99	80
TK2009112601-55B		mantle	0.900365	0.074135	0.103273	0.004918	0.578	0.063231	0.004247	652	40	634	29	716	150	103	0.42	170	25	73	21	24	20
TK2009112601-55C		rim	0.815548	0.047895	0.09628	0.004364	0.772	0.061435	0.002294	606	27	593	26	654	82	102	0.11	678	97	76	22	84	68
TK2009112601-56A	inc in garnet	core	0.727565	0.058196	0.093144	0.004553	0.589	0.056652	0.003663	555	35	574	26	478	150	99	0.29	288	33	66	19	28	23
TK2009112601-56B		mantle	0.818644	0.042554	0.097995	0.004392	0.862	0.060589	0.001596	607	24	603	26	625	58	101	0.20	1624	233	321	92	208	169
TK2009112601-57A	inc in garnet	rim	0.766414	0.042563	0.09441	0.004254	0.811	0.058877	0.001911	578	25	582	25	563	72	99	0.28	1005	144	282	81	126	102
TK2009112601-57B		rim	0.742705	0.04776	0.091452	0.004183	0.711	0.058901	0.002662	564	28	564	25	563	102	100	0.23	482	69	112	32	58	47
TK2009112601-61A	in matrix	rim	0.790243	0.048438	0.092562	0.004552	0.450	0.061919	0.00339	591	28	571	15	671	122	104	0.30	279	18	184	11	36	24
TK2009112601-61B		rim	0.927303	0.047488	0.09752	0.004369	0.875	0.068964	0.001711	666	25	600	26	898	52	111	0.10	1714	246	167	48	218	177
TK2009112601-61C		core	0.881331	0.088621	0.100217	0.004993	0.495	0.063781	0.005571	642	49	616	29	734	197	104	0.38	101	15	39	11	14	11
TK2009112601-62A	in matrix	rim	0.799504	0.026226	0.094873	0.002312	0.743	0.061119	0.001342	597	15	584	14	643	48	102	0.05	2506	165	118	16	311	211
TK2009112601-62B		mantle	0.773234	0.06798	0.095387	0.002997	0.357	0.058792	0.004827	582	40	587	18	559	190	99	0.37	122	8	45	6	16	11
TK2009112601-62C		rim	0.858849	0.046529	0.100255	0.002672	0.492	0.062131	0.002931	629	26	616	16	679	104	102	0.35	353	23	122	16	52	35
TK2009112601-63A	in matrix	core	0.763853	0.027361	0.09456	0.002327	0.687	0.058587	0.001525	576	16	582	14	552	58	99	0.16	1605	106	256	34	204	138
TK2009112601-63B		rim	0.765639	0.033241	0.095455	0.002416	0.583	0.058173	0.002052	577	19	588	14	536	79	98	0.23	755	50	174	23	98	67
TK2009112601-65	inc in garnet	mantle	0.799718	0.041597	0.096685	0.004441	0.923	0.05999	0.00201	597	24	595	27	603	44	100	0.08	4058	444	321	70	501	377
TK2009112601-66	inc in garnet	core	0.828164	0.047665	0.10013	0.004845	0.841	0.059986	0.001869	613	27	615	28	603	69	100	0.36	1100	120	397	87	151	113
TK2009112601-67	inc in garnet	core	0.804444	0.042348	0.096049	0.004615	0.913	0.060744	0.00136	599	24	591	27	630	47	101	0.08	3161	346	241	53	388	292
TK2009112601-68A	inc in garnet	core	0.747001	0.052567	0.091847	0.004535	0.702	0.058987	0.002958	566	31	566	27	567	113	100	0.25	413	45	102	22	51	38
TK2009112601-68B		rim	0.757836	0.05065	0.092957	0.004625	0.666	0.059128	0.003299	573	33	573	27	572	126	100	0.41	324	36	132	29	42	32
TK2009112601-69	in matrix	mantle	0.873261	0.048714	0.103873	0.005014	0.865	0.060973	0.001705	637	27	637	29	638	61	100	0.37	1371	150	511	112	196	148
TK2009112601-70A	in matrix	core	0.772304	0.041242	0.094678	0.004553	0.901	0.059161	0.001373	581	24	583	27	573	51	100	0.05	2593	284	140	31	311	234
TK2009112601-70B		core	0.809203	0.071248	0.096415	0.004938	0.581	0.060571	0.004364	602	41	593	29	635	162	101	0.33	180	20	60	13	24	18
TK2009112601-70C		rim	0.751315	0.044851	0.09158	0.004445	0.813	0.0595	0.002068	569	26	565	26	585	77	101	0.24	933	102	220	48	114	86
TK2009112601-71A	in garnet b.d.	mantle	0.737393	0.079685	0.089201	0.004756	0.493	0.059955	0.005635	561	48	551	28	602	218	102	0.28	113	12	32	7	14	11
TK2009112601-71B	in garnet b.d.	core	0.772689	0.042369	0.094535	0.004556	0.879	0.05928	0.001551	581	25	582	27	577	58	100	0.31	1846	202	570	125	236	177
TK2009112601-73	in matrix	core	0.789002	0.041562	0.095802	0.004603	0.912	0.059731	0.00129	591	24	590	27	594	47	100	0.08	3179	348	258	56	390	293
TK2009112601-74	in matrix	mantle	0.764374	0.033423	0.09309	0.002748	0.675	0.059552	0.001921	577	19	574	16	587	72	100	0.13	2454	231	124	23	297	206
TK2009112601-75A	in matrix	rim	0.743313	0.035873	0.090293	0.002703	0.620	0.059706	0.00226	564	21	557	16	593	84	101	0.10	1253	118	129	24	149	103
TK2009112601-75B		rim	0.766999	0.047878	0.094104	0.002958	0.505	0.059345	0.003184	580	28	580	17	580	121	100	0.24	423	40	102	19	54	38
TK2009112601-75C		mantle	0.754307	0.043313	0.090164	0.002796	0.533	0.060675	0.00299	571	26	557	17	628	110	103	0.33	542	51	180	34	68	47
TK2009112601-76A	in matrix	core	0.903963	0.043657	0.112273	0.00336	0.621	0.058524	0.00221	655	24	686	20	549	85	95	0.10	1035	97	108	20	153	106
TK2009112601-76B		rim	0.777846	0.032673	0.095762	0.002812	0.699	0.058911	0.001769	584	19	590	17	564	67	99	0.29	3758	354	240	45	469	325
TK2009112601-77A	in matrix	rim	0.729311	0.05081	0.092435	0.002981	0.463	0.057224	0.003534	556	30	570	18	500	142	98	0.25	314	30	78	15	40	28
TK2009112601-77B		mantle	0.857035	0.068791	0.102049	0.00346	0.422	0.06091	0.004431	629	38	626	20	636	165	100	0.13	183	17	65	12	27	18
TK2009112601-77C		core	0.869925	0.036949	0.103534	0.00346	0.693	0.060939	0.001867	636	20	635	18	637	67	100	0.42	2933	284	1228	231	432	300
TK2009112601-78A		rim	0.921466	0.066634	0.11078	0.003632	0.453	0.060328	0.003888	663	36	677	21	615	146	98	0.52	225	21	117	22	36	25
TK2009112601-78B	in matrix	core	1.462504	0.059643	0.123014	0.003608	0.719	0.086227	0.002443	915	25	748	21	1343	56	122	0.10	3424	322	355	67	588	408
TK2009112601-78C		rim	0.741325	0.041328	0.093509	0.002677	0.550	0.057498	0.002677	563	24	576	17	511	106	98	0.20	645	61	129	24	81	56
TK2009113001B-11A	in matrix	core	1.33761	0.11176	0.151423	0.004379	0.346	0.064067	0.005022	862	50	909	25	744	175	94.9	0.54	93	12	50	13	21	14
TK2009113001B-11B		rim	0.778667	0.035572	0.093726	0.002105	0.492	0.060254	0.002393	585	21	578	12	613	88	101	0.05	773	96	41	10	96	62
TK2009113001B-12A		rim	0.794271	0.059338	0.098115	0.002616	0.357	0.058713	0.004097	594	34	603	15	556	160	98	1.12	199	25	223	55	33	21
TK2009113001B-12B		core	0.813669	0.029937	0.096636	0.002074	0.583	0.061067	0.001825	605	17	595	12	642	66	102	0.05	1786	222	90	22	230	148
TK2009113001B-12C		core	1.106515	0.065009	0.122958	0.003017	0.418	0.065268	0.003484	756	32	748	17	783	116	101	0.40	263	33	122	30	48	31
TK2009113001B-17D		rim	0.737288	0.073081	0.09493	0.00345	0.367	0.056329	0.005194	561	44	585	20	465	218	95.9	1.29	125	12	161	30	20	14
TK2009113001B-21A	inc in biotite	core	1.227391	0.050707	0.133708	0.002953	0.535	0.066577	0.002325	813	23	809	17	825	75	101	0.48	714	89	344	85	141	91
TK2009113001B-21B	inc in garnet	rim	1.158487	0.050569	0.127369	0.002849	0.512	0.065967	0.002473	781	24	773	16	805	81	101	0.69	615	76	426	106	121	78
TK2009113001B-21C		rim	0.700768	0.050531	0.094408	0.004017	0.359	0.053835	0.003608	539	31	582	14	364	159	92.7	1.01	246	31	247	61	38	25
TK2009113001B-22A	in matrix	rim	0.811972	0.068571	0.097048	0.002769	0.338	0.060681	0.004823	604	39	597	16	628	181	101	1.10	148	18	162	40	25	16
TK2009113001B-22B	in matrix	mantle	0.786791	0.035351	0.099857	0.002227	0.496	0.057145	0.002229	589	20	614	13	497	88	96.1	0.09	1000	140	71	18	108	70
TK2009113001B-23A	in garnet	rim	0.846684	0.062113	0.096741	0.002593	0.365	0.063476	0.004335	623	35	595	15	724	152	104.6	0.96	197	24	190	47	31	20
TK2009113001B-23B	in matrix	core	1.003796	0.040556	0.115087	0.002521	0.542	0.063258	0.002148	706	21	702	15	717	74	101	0.31	947	118	297	74	155	100
TK2009113001B-27A	in matrix	rim	1.153538	0.045532	0.12762	0.002787	0.553	0.065556	0.002156	779	22	774	16	792	71	101	0.12	913	113	112	28	159	102
TK2009113001B-27B	in matrix	rim	1.282152	0.07019	0.133094	0.003718	0.511	0.069868	0.003286	838	32	805	21	924	100	104.0	0.20	277	31	57	13	51	34
TK2009113001B-27C		mantle	1.202825	0.04595	0.136023	0.00352	0.677	0.064134	0.001802	802	21	822	20	746	61	97.5	0.04	1225	137	51	12	221	133
TK2009113001B-2A		core	1.108003	0.061442	0.124212	0.003348	0.486	0.064696	0.003135	757	30	755	19	764	106	100	0.58	259	17	151	20	48	32
TK2009113001B-2B	in matrix	rim	0.818233	0.054712	0.095602	0.002713	0.424	0.062074	0.003758	607	31	589	16	677	135	103.1	0.17	218	14	38	5	28	19
TK2009113001B-2C		mantle	1.103481	0.045407	0.126742	0.003193	0.612	0.063146	0.002054	755	22	769	18	713	71	98	0.28	637	42	179	24	112	76
TK2009113001B-3A		rim	0.71351	0.041963	0.089294	0.002416	0.460	0.057953	0.003026	547	25	551	14	528	119	99	0.38	340	22	130	17	43	29
TK2009113001B-3B		mantle	0.947184	0.033726	0.11128	0.00274	0.692	0.061733	0.001588	677	18	680	16	665	56	99	0.11	1342	89	54	7	195	132
TK2009113001B-3C		rim	1.163294	0.055279	0.12822	0.00333	0.547	0.065268	0.002618	784	26	778	19	800	86	101	0.57	381	25	216	29	77	48
TK2009113001B-4A		core	1.266264	0.061775	0.140711	0.00380	0.555	0.065268	0.002627	831	28	849	22	783	88	98	0.41	399	45	163	37	81	48
TK2009113001B-4B	in matrix	rim	0.788545	0.063174	0.097342	0.003019	0.387	0.058752	0.00434	590	37	599	18	558	170	99	1.51	163	18	246	55	29	17
TK2009113001B-5A		mantle	1.050245	0.061287	0.118741	0.00335	0.483	0.064149	0.003237	729	31	723	19	747	112	101	0.64	277	31	178	40	50	30
TK2009113001B-5B		core	1.262501	0.075225	0.139266	0.003844	0.463	0.065749	0.003472	829	34	841	22	798	115	99	0.49	189	13	92	12	39	26
TK2009113001B-7A		rim	0.784725	0.047907	0.096393	0.00273	0.464	0.059043	0.003193	588	28	593	16	569	122	99	0.85	324	36	276	62	50	30
TK2009113001B-7B		core	1.136167	0.044608	0.12771	0.003305	0.662	0.064777	0.001907	771	21	772	19	767	63	100	0.13	1108	124	140	31	191	115
TK2009113001B-7C		mantle	0.80033	0.050941	0.09914	0.00284	0.450	0.058549	0.00328	597	29	609	17	550	129	98	0.34	322	32	267	60	45	27
TK2009113001B-8A	in matrix	rim	0.767331	0.060032	0.09714	0.002974	0.391	0.058574	0.004125	578	35	598	17	503	167	96.8	0.96	176	20	169	38	28	17
TK2009113001B-8B	in matrix	rim	0.983365	0.061772	0.110959	0.003198	0.459	0.064276	0.003888	695	32	678	19	751	123	102.5	0.28	242	27	67	15	38	23
TK2009113001B-9A	in matrix	mantle	1.171108	0.066864	0.124656	0.003515	0.494	0.068137	0.003383	787	32	757	20	873	106	103.9	0.61	267	30	162	36	51	30
TK2009113001B-9B	in matrix	mantle	1.187953	0.044968	0.133414	0.003448	0.683	0.06458	0.001786	795	21	807	20	761	59	98	0.43	1314	147	562	126	255	153
TK2009113001B-9C		rim	1.141784	0.044968	0.130672	0.003411	0.643	0.06372	0.001972	773	22	792	19	721	67	97.7	0.11	922	103	97	22	162	97
TK20113001G 10-1	inc in garnet	rim	0.899376	0.051048	0.099993	0.004146	0.730	0.065233	0.002529	651	28	614	24	782	84	106	0.09	567	82	33	5	57	9
TK20113001G 10-2	inc in garnet	rim	1.022433	0.045106	0.094269	0.003822	0.919	0.078662	0.001368	715	23	581	23	1164	35	123	0.02	2706	390	52	8	262	40
TK20113001G 10-3	inc in garnet	rim	1.053029	0.039198	0.112614	0.002590	0.618	0.067818	0.001985	730	20	688	15	863	62	106	0.05	493	143	23	5	54	15
TK20113001G 1-1	inc in garnet	rim	0.865671	0.039148	0.103290	0.002303	0.493	0.060785	0.002391	633	22	634	13	632	87	100	0.01	1064	155	13	2	104	14
TK20113001G 1-2	inc in garnet	mantle	0.886832	0.044025	0.102939	0.004207	0.823	0.062483	0.001760	645	24	632	25	691	61	102	0.00	1105	159	4	1	111	17
TK20113001G 2-1	inc in garnet	core	0.908821	0.046630	0.106231	0.004359	0.799	0.061989	0.001913	656	25	651	25	674	67	101	0.00	893	129	1	0	93	14
TK20113001G 2-4	inc in garnet	rim	0.968519	0.035503	0.094355	0.002173	0.628	0.074446	0.002123	688	18	581	13	1054	59	118	0.07	569	165	42	9	53	15
TK20113001G 2-5	inc in garnet	rim	0.865268	0.031424	0.095150	0.001975	0.566	0.065954	0.001975	633	17	586	12	805	64	108	0.07	523	61	38	4	49	6
TK20113001G 7-1	inc in garnet	core	0.740215	0.027448	0.092413	0.002109	0.615	0.058093	0.001698	563	16	570	12	533	64	99	0.05	697	202	35	7	62	17
TK20113001G 7-3	inc in garnet	rim	1.010486	0.033706	0.116285	0.002624	0.476	0.062492	0.001548	709	17	709	15	709	53	100	0.05	736	213	34	7	82	22
TK20113001G 7-3	inc in garnet	rim	1.575276	0.122457	0.166619	0.004696	0.404	0.076492	0.004875	1030	46	993	26	1108	133	104	0.18	118	16	24	5	11	3
TK20113001G 7-4	inc in garnet	rim	0.937309	0.029901	0.095398	0.001923	0.632	0.071260	0.001762	671	16	587	11	965	51	114	0.04	723	84	28	3	68	8
TK20113001G 8-1	inc in garnet	core	0.821724	0.045807	0.095651	0.003953	0.741	0.062307	0.002331	609	26	589	23	685	82	103	-	666	96	-	-	63	10
TK20113001G 8-2	inc in garnet	core	2.070687	0.091097	0.188508	0.007644	0.922	0.079668	0.00360	1139	31	1113	42	1189	34	102	0.06	1395	201	366	54	279	43
TK20113001G 111-1	in garnet b.d.	mantle	1.539872	0.047903	0.147966	0.003120	0.678	0.075478	0.001726	946	19	890	18	1081	47	106	0.18	1204	124	221	16	188	18
TK20113001G 111-2	in garnet b.d.	rim	0.784291	0.034890	0.097972	0.002183	0.501	0.058060	0.002236	588	20	603	13	532	87	98	0.04	699	72	30	2	68	7
TK20113001G 111-3	in garnet b.d.	rim	0.747601	0.033970	0.094491	0.002114	0.492	0.057382	0.002220	567	20	582	12	506	89	97	0.09	692	71	63	4	66	5
TK20113001G 113-1	inc in biotite	core	1.308895	0.059958	0.116030	0.002689	0.506	0.081855	0.003233	850	27	708	16	1241	79	120	0.16	406	84	17	4	50	5
TK20113001G 113-1	in matrix	core	1.881409	0.054977	0.184617	0.003855	0.715	0.073911	0.001511	1075	20	1092	21	1038	42	98	0.13	1321	136	437	31	265	25
TK20113001G 113-2	in matrix	core	1.853040	0.075884	0.183856	0.004104	0.545	0.073098	0.002510	1065	27	1088	22	1017	71	98	0.18	386	40	69	5	74	7
TK20113001G 139-1	in garnet b.d.	rim	0.765100	0.029278	0.093823	0.002027	0.565	0.059144	0.001868	577	17	578	12	572	70	100	0.17	1110	114	23	2	103	10
TK20113001G 139-2	in garnet b.d.	mantle	0.974806	0.043874	0.095060	0.002181	0.507	0.073907	0.002368	691	23	589	13	1039	80	117	0.07	562	58	41	3	56	6
TK20113001G 139-3	in garnet b.d.	rim	1.157245	0.036667	0.112158	0.002370	0.667	0.074833	0.001767	781	17	685	14	1064	48	114	0.03	1478	152	47	3	172	17
TK20113001G 14-1	inc in garnet	core	1.491455	0.061276	0.151684	0.005733	0.920	0.071313	0.001148	927	25	910	32	966	33	102	0.24	5099	416	1242	129	835	73
TK20113001G 14-2	inc in garnet	rim	0.909514	0.046307	0.106493	0.004102	0.757	0.061942	0.002062	657	25	652	24	672	73	101	0.01	913	74	23	2	98	9
TK20113001G 175-1	inc in sillimanite	core	1.490070	0.042759	0.153073	0.003130	0.634	0.070600	0.001396	926	18	918	11	946	41	101	0.04	1820	187	161	11	283	27
TK20113001G 175-2	inc in sillimanite	mantle	0.769230	0.027397	0.093321	0.001992	0.599	0.059783	0.001704	579	16	575	12	596	63	101	0.04	1395	144	54	4	130	13
TK20113001G 175-3	inc in sillimanite	rim	0.801347	0.041700	0.093132	0.002179	0.450	0.062405	0.002901	598	24	574	13	688	102	104	0.03	460	47	40	3	43	4
TK20113001G 18-1	in garnet b.d.	core	1.207844	0.064420	0.132689	0.005225	0.738	0.066020	0.002371	804	30	803	30	807	77	100	0.13	625	60	79	3	87	8
TK20113001G 18-2	in garnet b.d.	mantle	0.788112	0.040719	0.093454	0.003660	0.758	0.061163	0.002061	590	23	576	22	645	74	102	0.10	1136	109	56	2	108	10
TK20113001G 18-3	in garnet b.d.	rim	0.794864	0.049268	0.093454	0.003703	0.646	0.061379	0.002685	594	28	579	22	653	105	103	0.14	484	46	22	1	46	4
TK20113001G 182-1	inc in sillimanite	rim	2.055492	0.057176	0.188102	0.003903	0.746	0.079254	0.001468	1134	19	1111	21	1178	37	102	1.11	1835	337	2029	347	432	86
TK20113001G 184-1	inc in garnet overgrowing sillimanite	core	1.860032	0.072533	0.181679	0.004006	0.566	0.074253	0.002388	1067	26	1076	22	1048	66	99	0.40	506	93	201	34	103	20
TK20113001G 184-2	inc in garnet overgrowing sillimanite	core	1.495085	0.046437	0.146032	0.003003	0.628	0.074251	0.001588	928	19	932	20	920	85	100	0.20	417	76	85	15	66	13
TK20113001G 184-3	inc in garnet overgrowing sillimanite	core	0.808067	0.046032	0.091987	0.002220	0.424	0.063712	0.003288	601	26	567	13	732	113	106	0.09	280	51	76	8	41	5
TK20113001G 184-4	inc in garnet overgrowing sillimanite	core	1.294331	0.059205	0.098875	0.002320	0.513	0.094942	0.003637	843	27	608	14	1527	76	139	0.19	478	88	91	16	54	13
TK20113001G 184-5	inc in garnet overgrowing sillimanite	core	1.675727	0.079980	0.167780	0.003899	0.487	0.072437	0.003020	999	31	1000	22	998	87	100	0.18	318	58	88	15	57	11
TK20113001G 192-1	in garnet b.d.	core	1.651633	0.040849	0.156999	0.003206	0.826	0.076298	0.001064	990	16	940	18	1103	28	105	0.12	6366	1167	766	131	1060	209
TK20113001G 192-2	in garnet b.d.	rim	0.823632	0.029384	0.099030	0.002114	0.598	0.060321	0.001724	610	16	609	13	615	63	100	0.08	1475	270	68	12	147	29
TK20113001G 192-3	in garnet b.d.	rim	0.791947	0.039698	0.091759	0.002121	0.461	0.062600	0.002784	592	23	566	13	695	98	105	0.10	615	113	27	5	78	16
TK20113001G 194	in garnet b.d.	core	0.967043	0.049630	0.089689	0.002005	0.541	0.078200	0.002719	687	21	554	12	1152	71	124	0.01	822	151	10	2	78	16
TK20113001G 20-1	in garnet b.d.	core	1.524001	0.049630	0.157860	0.003344	0.650	0.070018	0.001732	940	20	945	19	929	52	100	0.12	1135	208	139	24	186	37
TK20113001G 20-2	in garnet b.d.	rim	1.006391	0.048569	0.097808	0.002277	0.482	0.074626	0.003155	707	25	602	13	1058	88	118	0.06	515	95	32	6	54	11
TK20113001G 20-3	in garnet b.d.	rim	0.759154	0.032658	0.095908	0.002117	0.513	0.057408	0.002120	574	19	590	12	507	83	97	0.07	899	165	66	11	87	17
TK20113001G 22-1	inc in biotite	core	2.400719	0.138378	0.205153	0.008238	0.697	0.084872	0.003509	1243	42	1203	44	1313	82	103	0.75	224	32	168	7	54	5
TK20113001G 25-1	in garnet b.d.	rim	0.816499	0.046978	0.092025	0.003654	0.690	0.064350	0.002679	606	27	568	22	753	90	107	0.05	639	61	33	1	60	6
TK20113001G 25-2	in garnet b.d.	rim	0.939109	0.054403	0.092969	0.003709	0.689	0.073271	0.003071	672	29	573	22	1021	87	117	-	549	52	-	-	70	6
TK20113001G 35-1	in matrix	rim	0.883405	0.048286	0.102045	0.003965	0.711	0.062787	0.002414	643	27	626	23	701	84	101	0.10	678	55	4	0	70	6
TK20113001G 26-1	in matrix	core	1.370360	0.066951	0.140976	0.005483	0.656	0.070500	0.002215	875	29	850	31	942	65	103	0.33	196	26	65	3	46	4
TK20113001G 35-2	in matrix	core	0.883020	0.053161	0.094975	0.003748	0.656	0.067431	0.003066	643	29	585	22	851	97	110	0.03	460	44	12	1	46	4
TK20113001G 35-1	in matrix	core	1.047205	0.061087	0.097704	0.003910	0.686	0.077736	0.003299	727	31	601	13	1140	87	121	0.10	482	46	47	2	53	5
TK20113001G 35-2	in matrix	rim	0.757653	0.046495	0.092878	0.003732	0.651	0.059144	0.002872	573	27	573	22	573	105	100	0.04	525	50	41	3	52	5
TK20113001G 49-1	in matrix	core	1.138704	0.044558	0.122445	0.003019	0.630	0.067448	0.002050	772	21	745	17	852	64	104	0.10	1021	43	17	0	125	5
TK20113001G 49-2	in matrix	rim	0.988029	0.053771	0.102564	0.003729	0.489	0.069863	0.003317	698	28	629	16	924	101	111	0.10	420	16	47	0	49	2
TK20113001G 49-3	in matrix	rim	0.753095	0.049242	0.089904	0.003630	0.618	0.060753	0.003124	570	29	555	22	631	115	103	0.10	421	40	40	3	39	2
TK20113001G 51-1	in matrix	core	1.004553	0.062805	0.091972	0.003827	0.587	0.079216	0.003772	706	32	567	12	1178	97	124	0.09	384	37	19	0	45	4
TK20113001G 51-2	in matrix	rim	0.809734	0.041299	0.092910	0.003717	0.626	0.063039	0.002730	602	25	573	22	709	110	106	0.13	413	39	51	4	42	4
TK20113001G 51-3	in matrix	core	0.764170	0.040067	0.093768	0.003684	0.732	0.057714	0.002113	566	24	578	22	519	82	98	0.13	959	92	36	2	90	8
TK20113001G 51-4	in matrix	core	0.777576	0.042596	0.095289	0.003783	0.682	0.059183	0.002447	584	26	587	17	574	105	100	0.01	514	96	4	0	51	4
TK20113001G 78-1	in matrix	core	1.077080	0.041333	0.120362	0.002954	0.640	0.064902	0.001915	742	20	733	17	771	63	101	0.10	1177	49	45	1	142	5
TK20113001G 78-2	in matrix	core	0.875802	0.047257	0.095402	0.003750	0.581	0.066571	0.003150	639	26	587	15	781	105	109	0.14	671	17	43	1	77	3
TK20113001G 84-1	in biotite	core	1.046815	0.042192	0.116211	0.002876	0.614	0.065332	0.002078	727	21	709	17	785	68	103	0.10	971	41	33	1	114	4
TK20113001G 84-2	in matrix	rim	0.810491	0.033538	0.099870	0.003375	0.602	0.058859	0.001922	628	20	634	15	562	74	98	0.26	1109	47	65	1	111	4
TK20113001G 84-3	in biotite	core	0.856733	0.055323	0.093375	0.002526	0.500	0.066547	0.003560	628	20	634	13	562	45	98	0.17	562	54	60	1	119	5
TK20113001G 87-1	in matrix	rim	0.747433	0.081129	0.094254	0.004820	0.634	0.077462	0.002341	1140	27	1144	26	1133	61	100	0.28	575	24	141	3	119	5
TK20113001G 87-2	in matrix	core	1.942353	0.068773	0.192390	0.004979	0.687	0.073240	0.001884	1096	24	1134	30	1021	53	93	0.28	444	292	6	11	67	5
TK20113001G 87-3	in matrix	rim	0.783073	0.043728	0.092498	0.002449	0.474	0.061400	0.003019	587	25	570	14	653	109	103	0.11	435	18	47	1	41	2
TK20113001G 87-4	in matrix	core	0.831999	0.045877	0.092648	0.002610	0.475	0.061169	0.002997	615	26	606	15	645	109	101	0.17	6	10	6	1	63	4
TK20113001G 92-1	in garnet b.d.	rim	0.725471	0.043265	0.092910	0.002247	0.405	0.056631	0.003087	554	26	573	13	477	125		0.10	362	37	35	3	34	3
TK20113001G 92-2	in garnet b.d.	core	1.910877	0.102343	0.190619	0.005093	0.499	0.072705	0.003375	1085	36	1125	28	1006	97	96	0.41	206	9	85	2	63	2
TK20113001G 92-3	in garnet b.d.	mantle	0.834318	0.035060	0.102007	0.002533	0.591	0.059320	0.002011	616	20	626	17	579	75	101	0.01	1015	43	14	0	103	4

Table 2 Kawakami et al.